EUROPEAN ORGANISATION FOR NUCLEAR RESEARCH

CERN-PPE/96-155
6 November 1996

Analysis of hadronic final states and the photon structure function F_2^γ in deep inelastic electron-photon scattering at LEP

The OPAL Collaboration

Abstract

Deep inelastic electron-photon scattering is studied in the Q^2 ranges from 6 to 30 GeV^2 and from 60 to 400 GeV^2 using the full sample of LEP data taken with the OPAL detector at centre-of-mass energies close to the Z^0 mass, with an integrated luminosity of 156.4 pb^{-1}. Energy flow distributions and other properties of the measured hadronic final state are compared with the predictions of Monte Carlo models, including HERWIG and PYTHIA. Sizeable differences are found between the data and the models, especially at low values of the scaling variable x. New measurements are presented of the photon structure function $F_2^\gamma(x, Q^2)$, allowing for the first time for uncertainties in the description of the final state by different Monte Carlo models. The differences between the data and the models contribute significantly to the systematic errors on F_2^γ. The slope $\mathrm{d}(F_2^\gamma/\alpha)/\mathrm{d}\ln Q^2$ is measured to be $0.13^{+0.06}_{-0.04}$.

(Submitted to Zeitschrift für Physik C)

The OPAL Collaboration

K. Ackerstaff[8], G. Alexander[23], J. Allison[16], N. Altekamp[5], K. Ametewee[25], K.J. Anderson[9], S. Anderson[12], S. Arcelli[2], S. Asai[24], D. Axen[29], G. Azuelos[18,a], A.H. Ball[17], E. Barberio[8], R.J. Barlow[16], R. Bartoldus[3], J.R. Batley[5], J. Bechtluft[14], C. Beeston[16], T. Behnke[8], A.N. Bell[1], K.W. Bell[20], G. Bella[23], S. Bentvelsen[8], P. Berlich[10], S. Bethke[14], O. Biebel[14], V. Blobel[27], I.J. Bloodworth[1], J.E. Bloomer[1], M. Bobinski[10], P. Bock[11], H.M. Bosch[11], M. Boutemeur[34], B.T. Bouwens[12], S. Braibant[12], R.M. Brown[20], H.J. Burckhart[8], C. Burgard[8], R. Bürgin[10], P. Capiluppi[2], R.K. Carnegie[6], A.A. Carter[13], J.R. Carter[5], C.Y. Chang[17], D.G. Charlton[1,b], D. Chrisman[4], P.E.L. Clarke[15], I. Cohen[23], J.E. Conboy[15], O.C. Cooke[16], M. Cuffiani[2], S. Dado[22], C. Dallapiccola[17], G.M. Dallavalle[2], S. De Jong[12], L.A. del Pozo[8], K. Desch[3], M.S. Dixit[7], E. do Couto e Silva[12], M. Doucet[18], E. Duchovni[26], G. Duckeck[34], I.P. Duerdoth[16], J.E.G. Edwards[16], P.G. Estabrooks[6], H.G. Evans[9], M. Evans[13], F. Fabbri[2], P. Fath[11], F. Fiedler[27], M. Fierro[2], H.M. Fischer[3], R. Folman[26], D.G. Fong[17], M. Foucher[17], A. Fürtjes[8], P. Gagnon[7], A. Gaidot[21], J.W. Gary[4], J. Gascon[18], S.M. Gascon-Shotkin[17], N.I. Geddes[20], C. Geich-Gimbel[3], F.X. Gentit[21], T. Geralis[20], G. Giacomelli[2], P. Giacomelli[4], R. Giacomelli[2], V. Gibson[5], W.R. Gibson[13], D.M. Gingrich[30,a], D. Glenzinski[9], J. Goldberg[22], M.J. Goodrick[5], W. Gorn[4], C. Grandi[2], E. Gross[26], J. Grunhaus[23] M. Gruwé[8], C. Hajdu[32], G.G. Hanson[12], M. Hansroul[8], M. Hapke[13], C.K. Hargrove[7], P.A. Hart[9], C. Hartmann[3], M. Hauschild[8], C.M. Hawkes[5], R. Hawkings[8], R.J. Hemingway[6], M. Herndon[17], G. Herten[10], R.D. Heuer[8], M.D. Hildreth[8], J.C. Hill[5], S.J. Hillier[1], T. Hilse[10], P.R. Hobson[25], R.J. Homer[1], A.K. Honma[28,a], D. Horváth[32,c], R. Howard[29], R.E. Hughes-Jones[16], D.E. Hutchcroft[5], P. Igo-Kemenes[11], D.C. Imrie[25], M.R. Ingram[16], K. Ishii[24], A. Jawahery[17], P.W. Jeffreys[20], H. Jeremie[18], M. Jimack[1], A. Joly[18], C.R. Jones[5], G. Jones[16], M. Jones[6], R.W.L. Jones[8], U. Jost[11], P. Jovanovic[1], T.R. Junk[8], D. Karlen[6], K. Kawagoe[24], T. Kawamoto[24], R.K. Keeler[28], R.G. Kellogg[17], B.W. Kennedy[20], B.J. King[8], J. Kirk[29], S. Kluth[8], T. Kobayashi[24], M. Kobel[10], D.S. Koetke[6], T.P. Kokott[3], M. Kolrep[10], S. Komamiya[24], T. Kress[11], P. Krieger[6], J. von Krogh[11], P. Kyberd[13], G.D. Lafferty[16], H. Lafoux[21], R. Lahmann[17], W.P. Lai[19], D. Lanske[14], J. Lauber[15], S.R. Lautenschlager[31], J.G. Layter[4], D. Lazic[22], A.M. Lee[31], E. Lefebvre[18], D. Lellouch[26], J. Letts[2], L. Levinson[26], C. Lewis[15], S.L. Lloyd[13], F.K. Loebinger[16], G.D. Long[17], M.J. Losty[7], J. Ludwig[10], A. Malik[21], M. Mannelli[8], S. Marcellini[2], C. Markus[3], A.J. Martin[13], J.P. Martin[18], G. Martinez[17], T. Mashimo[24], W. Matthews[25], P. Mättig[3], W.J. McDonald[30], J. McKenna[29], E.A. Mckigney[15], T.J. McMahon[1], A.I. McNab[13], R.A. McPherson[8], F. Meijers[8], S. Menke[3], F.S. Merritt[9], H. Mes[7], J. Meyer[27], A. Michelini[2], G. Mikenberg[26], D.J. Miller[15], R. Mir[26], W. Mohr[10], A. Montanari[2], T. Mori[24], M. Morii[24], U. Müller[3], K. Nagai[26], I. Nakamura[24], H.A. Neal[8], B. Nellen[3], B. Nijjhar[16], R. Nisius[8], S.W. O'Neale[1], F.G. Oakham[7], F. Odorici[2], H.O. Ogren[12], N.J. Oldershaw[16], T. Omori[24], M.J. Oreglia[9], S. Orito[24], J. Pálinkás[33,d], G. Pásztor[32], J.R. Pater[16], G.N. Patrick[20], J. Patt[10], M.J. Pearce[1], S. Petzold[27], P. Pfeifenschneider[14], J.E. Pilcher[9], J. Pinfold[30],

D.E. Plane[8], P. Poffenberger[28], B. Poli[2], A. Posthaus[3], H. Przysiezniak[30], D.L. Rees[1], D. Rigby[1], S. Robertson[28], S.A. Robins[13], N. Rodning[30], J.M. Roney[28], A. Rooke[15], E. Ros[8], A.M. Rossi[2], M. Rosvick[28], P. Routenburg[30], Y. Rozen[22], K. Runge[10], O. Runolfsson[8], U. Ruppel[14], D.R. Rust[12], R. Rylko[25], K. Sachs[10], E.K.G. Sarkisyan[23], M. Sasaki[24], C. Sbarra[2], A.D. Schaile[34], O. Schaile[34], F. Scharf[3], P. Scharff-Hansen[8], P. Schenk[27], B. Schmitt[8], S. Schmitt[11], M. Schröder[8], H.C. Schultz-Coulon[10], M. Schulz[8], M. Schumacher[3], P. Schütz[3], W.G. Scott[20], T.G. Shears[16], B.C. Shen[4], C.H. Shepherd-Themistocleous[8], P. Sherwood[15], G.P. Siroli[2], A. Sittler[27], A. Skillman[15], A. Skuja[17], A.M. Smith[8], T.J. Smith[28], G.A. Snow[17], R. Sobie[28], S. Söldner-Rembold[10], R.W. Springer[30], M. Sproston[20], A. Stahl[3], M. Steiert[11], K. Stephens[16], J. Steuerer[27], B. Stockhausen[3], D. Strom[19], F. Strumia[8], P. Szymanski[20], R. Tafirout[18], S.D. Talbot[1], S. Tanaka[24], P. Taras[18], S. Tarem[22], M. Thiergen[10], M.A. Thomson[8], E. von Törne[3], S. Towers[6], I. Trigger[18], T. Tsukamoto[24], E. Tsur[23], A.S. Turcot[9], M.F. Turner-Watson[8], P. Utzat[11], R. Van Kooten[12], G. Vasseur[21], M. Verzocchi[10], P. Vikas[18], M. Vincter[28], E.H. Vokurka[16], F. Wäckerle[10], A. Wagner[27], C.P. Ward[5], D.R. Ward[5], J.J. Ward[15], P.M. Watkins[1], A.T. Watson[1], N.K. Watson[7], P.S. Wells[8], N. Wermes[3], J.S. White[28], B. Wilkens[10], G.W. Wilson[27], J.A. Wilson[1], G. Wolf[26], S. Wotton[5], T.R. Wyatt[16], S. Yamashita[24], G. Yekutieli[26], V. Zacek[18],

[1]School of Physics and Space Research, University of Birmingham, Birmingham B15 2TT, UK
[2]Dipartimento di Fisica dell' Università di Bologna and INFN, I-40126 Bologna, Italy
[3]Physikalisches Institut, Universität Bonn, D-53115 Bonn, Germany
[4]Department of Physics, University of California, Riverside CA 92521, USA
[5]Cavendish Laboratory, Cambridge CB3 0HE, UK
[6] Ottawa-Carleton Institute for Physics, Department of Physics, Carleton University, Ottawa, Ontario K1S 5B6, Canada
[7]Centre for Research in Particle Physics, Carleton University, Ottawa, Ontario K1S 5B6, Canada
[8]CERN, European Organisation for Particle Physics, CH-1211 Geneva 23, Switzerland
[9]Enrico Fermi Institute and Department of Physics, University of Chicago, Chicago IL 60637, USA
[10]Fakultät für Physik, Albert Ludwigs Universität, D-79104 Freiburg, Germany
[11]Physikalisches Institut, Universität Heidelberg, D-69120 Heidelberg, Germany
[12]Indiana University, Department of Physics, Swain Hall West 117, Bloomington IN 47405, USA
[13]Queen Mary and Westfield College, University of London, London E1 4NS, UK
[14]Technische Hochschule Aachen, III Physikalisches Institut, Sommerfeldstrasse 26-28, D-52056 Aachen, Germany
[15]University College London, London WC1E 6BT, UK
[16]Department of Physics, Schuster Laboratory, The University, Manchester M13 9PL, UK
[17]Department of Physics, University of Maryland, College Park, MD 20742, USA

[18]Laboratoire de Physique Nucléaire, Université de Montréal, Montréal, Quebec H3C 3J7, Canada
[19]University of Oregon, Department of Physics, Eugene OR 97403, USA
[20]Rutherford Appleton Laboratory, Chilton, Didcot, Oxfordshire OX11 0QX, UK
[21]CEA, DAPNIA/SPP, CE-Saclay, F-91191 Gif-sur-Yvette, France
[22]Department of Physics, Technion-Israel Institute of Technology, Haifa 32000, Israel
[23]Department of Physics and Astronomy, Tel Aviv University, Tel Aviv 69978, Israel
[24]International Centre for Elementary Particle Physics and Department of Physics, University of Tokyo, Tokyo 113, and Kobe University, Kobe 657, Japan
[25]Brunel University, Uxbridge, Middlesex UB8 3PH, UK
[26]Particle Physics Department, Weizmann Institute of Science, Rehovot 76100, Israel
[27]Universität Hamburg/DESY, II Institut für Experimental Physik, Notkestrasse 85, D-22607 Hamburg, Germany
[28]University of Victoria, Department of Physics, P O Box 3055, Victoria BC V8W 3P6, Canada
[29]University of British Columbia, Department of Physics, Vancouver BC V6T 1Z1, Canada
[30]University of Alberta, Department of Physics, Edmonton AB T6G 2J1, Canada
[31]Duke University, Dept of Physics, Durham, NC 27708-0305, USA
[32]Research Institute for Particle and Nuclear Physics, H-1525 Budapest, P O Box 49, Hungary
[33]Institute of Nuclear Research, H-4001 Debrecen, P O Box 51, Hungary
[34]Ludwigs-Maximilians-Universität München, Sektion Physik, Am Coulombwall 1, D-85748 Garching, Germany

[a] and at TRIUMF, Vancouver, Canada V6T 2A3
[b] and Royal Society University Research Fellow
[c] and Institute of Nuclear Research, Debrecen, Hungary
[d] and Department of Experimental Physics, Lajos Kossuth University, Debrecen, Hungary

1 Introduction

The measurement of the photon structure function F_2^γ and especially of its evolution with the momentum transfer squared, Q^2, is a classic test of perturbative QCD [1]. The large range of Q^2 values accessible at the LEP collider makes it an ideal place to study this evolution.

This note describes a study of the properties of the hadronic final state and a measurement of F_2^γ in the Q^2 ranges from 6 to 30 GeV^2, and from 60 to 400 GeV^2 using a sample of singly-tagged two-photon events recorded by the OPAL detector from 1990

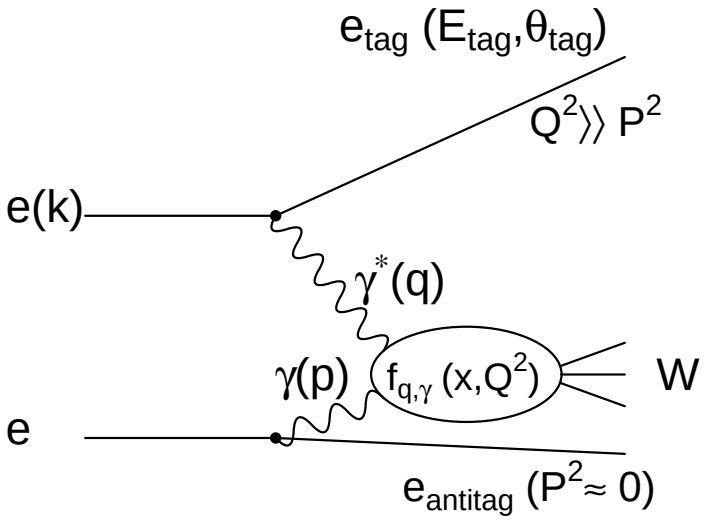

Figure 1: A diagram of deep inelastic electron-photon scattering.

to 1995. In the singly-tagged regime, the process $e^+e^- \rightarrow e^+e^- +$ hadrons can be regarded as deep inelastic scattering of an $e^{\pm}$ on a quasi-real photon[1], and the flux of quasi-real photons can be calculated using the equivalent photon approximation [2,3]. Figure 1 shows a diagram of this reaction. The four-vector of the incoming electron which radiates the virtual photon is denoted k. The four-vectors of the virtual photon and the quasi-real photon are represented by q and p, respectively. The symbol $f_{q,\gamma}(x, Q^2)$ represents the parton densities of the quasi-real photon. The cross-section for deep inelastic electron-photon scattering is expressed as [4],

$$\frac{d^2\sigma_{e\gamma\rightarrow eX}}{dxdQ^2} = \frac{2\pi\alpha^2}{x\,Q^4}\left[\left(1+(1-y)^2\right)F_2^{\gamma}(x,Q^2) - y^2 F_L^{\gamma}(x,Q^2)\right] \qquad (1)$$

where $Q^2 = -q^2$ is the negative value of the four-momentum squared of the virtual photon. The usual dimensionless variables of deep inelastic scattering, x and y, are defined as $x = \frac{Q^2}{2p\cdot q}$ and $y = \frac{p\cdot q}{p\cdot k}$. α is the fine structure constant. In the kinematic regime studied here ($y^2 \ll 2$) the contribution of the term proportional to $F_L^{\gamma}(x,Q^2)$ is small and therefore neglected.

In contrast to deep inelastic charged lepton-nucleon scattering, where the energies of both interacting particles are given, in deep inelastic electron-photon reactions the energy of the incoming quasi-real photon is not known. As a consequence of this, the

[1]The term singly-tagged denotes the situation where one electron, the one which radiates the virtual photon, is deep inelastically scattered and seen (tagged) in the detector, whereas the other electron, which radiates the quasi-real photon, leaves the detector unseen close to the beam direction. In this paper positrons are also referred to as electrons, and the electron and positron masses are neglected.

kinematics of the reaction in terms of x and Q^2 are not fully determined by measuring the four-vector of the tagged electron. The value of x has to be obtained by measuring the hadronic final state, which is only partly observed in the detector. This leads to a dependence of F_2^γ on the modelling of the hadronic final state by the Monte Carlo programs which are used in an unfolding process to relate the distributions of visible quantities to the underlying x distribution.

Most of the analyses formerly applied to determine F_2^γ used the FKP [5] formalism for light quarks to describe the "pointlike" part of F_2^γ, complemented by the "hadronic" part taken as the Vector Meson Dominance Model (VDM) parametrisation of the TPC/2γ [6] group and a heavy flavour contribution in the framework of the Quark Parton Model (QPM) [3]. A phenomenological parameter $p_{\rm t}^0$ was introduced to separate the perturbative, pointlike part from the non-perturbative, "hadronic" part of F_2^γ based on the transverse momentum of the quarks with respect to the photons in the rest frame of the hadronic system. This parameter was varied to give the best description of the data by the Monte Carlo model, which was then used to unfold F_2^γ. Several analyses using this strategy or a similar one have been published [6–13].

Now that deep inelastic electron-photon interactions have been implemented in the general purpose Monte Carlo programs HERWIG [14, 15] and PYTHIA [16, 17], it is no longer necessary to fit an empirical $p_{\rm t}^0$ parameter to the data before unfolding. In the analysis presented here, these generators are used for the first time to determine F_2^γ from the data.

2 The OPAL detector

The OPAL detector is described in detail elsewhere [18]; only the subdetectors which are most relevant for this analysis, namely the electromagnetic calorimeters and the tracking devices, are detailed below[2]. The OPAL detector has a uniform magnetic field of 0.435 T along the beam direction throughout the central tracking region, with electromagnetic and hadronic calorimetry and muon chambers outside the coil.

The forward detectors (FD) cover the θ region from 47 to 140 mrad at each end of the OPAL detector. They consist of cylindrical lead-scintillator calorimeters with a depth of 24 radiation lengths (X_0) divided azimuthally into 16 segments. The energy resolution for electromagnetic showers is $18\%/\sqrt{E}$, where E is in GeV. An array of three planes of proportional tubes buried in the calorimeter at a depth of 4 X_0 provides a precise shower position measurement, with a typical resolution of 3–4 mm, corresponding to 2.5 mrad in θ, and less than 3.5 mrad in ϕ. The acceptance of the FD covered the range in θ from 47 to 140 mrad from 1990 to 1992, and from 60 to

[2]In the OPAL right-handed coordinate system the x-axis points towards the centre of the LEP ring, the y-axis points upwards and the z-axis points in the direction of the electron beam. The polar angle θ and the azimuthal angle ϕ are defined with respect to the z-axis and x-axis, respectively.

140 mrad from 1993 onwards, after the installation of the small-angle silicon tungsten luminometer (SW) which covers the region in θ from 25 to 60 mrad. The space between the outer edge of the FD and the inner edge of the electromagnetic endcap calorimeter is filled by a small annular lead-scintillator calorimeter, the gamma catcher.

The endcap electromagnetic calorimeters are homogeneous devices composed of arrays of lead-glass blocks of 9.2×9.2 cm^2 cross-section and typically 22 X_0 in depth, giving good shower containment. The endcaps cover the angular range from 200 to 630 mrad. The energy resolution is typically $15\%/\sqrt{E}$, where E is in GeV, at angles above 350 mrad, but becomes worse closer to the edge of the detector.

Charged particles are detected by a silicon microvertex detector, a drift chamber vertex detector, and a jet chamber. Outside the jet chamber, but still in the magnetic field, lies a layer of drift chambers whose purpose is to improve the track reconstruction in the z-coordinate parallel to the beam direction. The resolution of the transverse momentum for charged particles is $\frac{\sigma p_t}{p_t} = \sqrt{0.02^2 + (0.0015\, p_t)^2}$ for $|\cos\theta| < 0.7$ and degrades for higher values of $|\cos\theta|$. Outside the solenoid is the electromagnetic barrel calorimeter, of similar construction to the endcaps described above.

3 Kinematics and data selection

The measurement of $F_2^\gamma(x, Q^2)$ involves the determination of x and Q^2 which can be obtained from the four-vectors of the tagged electron and the hadronic final state as follows:

$$Q^2 = 2\, E_\mathrm{b}\, E_\mathrm{tag}\, (1 - \cos\theta_\mathrm{tag}) \tag{2}$$

$$x = \frac{Q^2}{Q^2 + W^2 + P^2}\,. \tag{3}$$

E_tag and θ_tag are the energy and polar angle of the observed electron, E_b is the beam energy, and W the invariant mass of the hadronic final state. $P^2 = -p^2$ is the negative value of the virtuality of the quasi-real photon. For this singly-tagged sample, an antitag condition is applied (see list of cuts below). This ensures that P^2 is close to zero and it is neglected in evaluating x from Eq. 3.

The four-momentum of the hadronic system is calculated by summing over all charged particle tracks, assuming the pion mass, and calorimeter clusters without associated tracks, where quality criteria are applied to both the tracks and the clusters to ensure that they are well reconstructed [19].

The analysis uses all available data from the 1990 to 1995 LEP runs, with the e^+e^- centre-of-mass energies close to the Z^0 mass. The total integrated e^+e^- luminosity, determined from small-angle Bhabha scattering events, is 156.4 ± 1.7 pb^{-1}. The tagged electron is detected either in the forward detectors, ($Q^2 \approx 6 - 30\,\mathrm{GeV}^2$), or in the endcap electromagnetic calorimeters, ($Q^2 \approx 60 - 400\,\mathrm{GeV}^2$). These two samples are

subject to different selection criteria and are referred to as low-Q^2 and high-Q^2 samples. Candidate events for the process $\gamma^\star\gamma \to$ hadrons are required to satisfy criteria for the tagged electron as well as for the hadronic final state, in addition to several technical cuts to ensure good detector status and track quality. The event selection listed below has been designed to have a high efficiency for signal events and to reject background events, which mainly stem from the reactions $\gamma^\star\gamma \to \tau^+\tau^-$ and $\mathrm{Z}^0 \to$ hadrons. The cuts for the low-Q^2 sample are:

1. A tagged electron candidate is required which produces a cluster in a forward detector with energy $E_{\mathrm{tag}} \geq 0.775\,E_{\mathrm{b}}$ and polar angle $60 \leq \theta_{\mathrm{tag}} \leq 120$ mrad with respect to either of the beam directions.

2. The energy E_{a} of the most energetic cluster in the hemisphere opposite to the one which contains the tagged electron is restricted to $E_{\mathrm{a}} \leq 0.25\,E_{\mathrm{b}}$ (antitag requirement).

3. At least three tracks originating from the hadronic final state have to be present.

4. The visible invariant mass W_{vis} of the hadronic system, calculated as the mass of the four-momentum vector of the hadronic system as defined above, is required to be in the range $2.5 \leq W_{\mathrm{vis}} \leq 40$ GeV.

The cuts for the high-Q^2 sample are:

1. A tagged electron candidate is required which produces a cluster in an endcap calorimeter with energy $0.75\,E_{\mathrm{b}} \leq E_{\mathrm{tag}} \leq 1.15\,E_{\mathrm{b}}$ and polar angle $200 \leq \theta_{\mathrm{tag}} \leq 500$ mrad with respect to either of the beam directions.

2. The energy E_{a} of the most energetic cluster in the hemisphere opposite to the one which contains the tagged electron is restricted to $E_{\mathrm{a}} \leq 0.15\,E_{\mathrm{b}}$ (antitag requirement).

3. At least three tracks originating from the hadronic final state have to be present.

4. The visible invariant mass W_{vis} of the hadronic system, calculated as the mass of the four-momentum vector of the hadronic system as defined above, is required to be in the range $2.5 \leq W_{\mathrm{vis}} \leq 25$ GeV.

5. The balance in transverse momentum, $p_{\mathrm{t,bal}}$, with respect to the beam axis projected onto the tag plane (defined by the four-vectors of the beam electrons and the tagged electron) has to be smaller than 5 GeV.

6. The component of the momentum of the hadronic system which is transverse to the beam direction and the tag plane, $p_{\mathrm{t,out}}$, has to be smaller than 4 GeV.

7. The missing component of the momentum in the event along the beam axis, $p_{z,miss}$, has to be in the range $-0.5\,E_{\rm b} \leq p_{z,miss} \leq 0.5\,E_{\rm b}$. In calculating this quantity it is assumed that the untagged electron carries the full beam energy and escapes along the beam direction in the hemisphere which does not contain the tagged electron.

8. The energy deposited in the electromagnetic calorimeter in a cone in pseudo-rapidity and azimuthal angle (in radians) of size 0.5 about the direction of the tagged electron, excluding the cluster of the tagged electron, must be less than 2 GeV. The energy in a cone of the same size but in the direction opposite to the electron candidate cluster has to be less than 1 GeV.

The stricter cuts applied to events where the electron is tagged in the endcaps reflect the much lower signal to background ratio in this sample. With these cuts 5455 and 225 events, with average squared momentum transfers $\langle Q^2 \rangle$ of 13 GeV^2 and 135 GeV^2, are selected in the low-Q^2 and high-Q^2 samples, respectively. The accessible values in x range from 0.0025 to 0.994. Using sets of independent triggers, the trigger efficiency is evaluated to be 99.6% for the low-Q^2 sample and 100% for the high-Q^2 sample.

4 Monte Carlo generation and background estimates

A range of Monte Carlo generators has been used to simulate signal events, background events, and to check the calculations by comparing samples for the same process from more than one generator. All Monte Carlo events are passed through the OPAL detector simulation program [20] and the same reconstruction and analysis chain as the real data events.

Since the last OPAL publication on the photon structure function [7], the two general purpose generators HERWIG 5.8d and PYTHIA 5.718 have become available with the deep inelastic electron-photon scattering process included. They are used throughout this analysis. In addition, comparisons and systematic checks have been made using the generator F2GEN, which was developed based on the TWOGEN generator [21] for the previous OPAL analysis [7]. All these programs can generate events according to a chosen parametrisation of the photon structure function F_2^γ. The programs have been checked by comparing the cross-sections and distributions for samples generated with a QPM structure function with corresponding samples from the Vermaseren [22] generator using QED matrix elements and JETSET [16,23] fragmentation. All cross-sections agree well with each other in the selected region of Q^2 and W, with one exception. The cross-section in PYTHIA for W less than 5 GeV is 15 to 20% lower than the one predicted by HERWIG. The main features of the Monte Carlo models, as they were used in this analysis, are listed in table 1.

The most important difference between the signal-event generators is in the way

	HERWIG 5.8d	PYTHIA 5.718	F2GEN	Vermaseren
quark flavours	all	all	u,d,s	c
parton shower	initial + final	initial + final	final	final
fragmentation	cluster	string	string	string
SUE	yes/no	no	no	no
angular distrib.	matrix elements	matrix elements	pointlike/peripheral	pointlike
m_c [GeV]	1.8	1.35	–	1.6

Table 1: The most relevant features of the Monte Carlo models, as they were used in this analysis. SUE denotes the soft underlying event explained in the text.

in which they generate final state hadrons. Both HERWIG and PYTHIA incorporate QCD-inspired models of the emission of hard partons, followed by their own hadronisation processes, the JETSET string model in PYTHIA and the cluster model in HERWIG. This analysis is a first attempt to see whether they successfully predict the properties of final states in deep inelastic electron-photon scattering. The HERWIG generator provides the possibility of adding a "soft underlying event" (SUE) with a uniform rapidity plateau of extra hadrons from the photon remnant in addition to the partons from the perturbative process. In this analysis HERWIG is used without simulating the underlying event for the standard generation, as the inclusion of the underlying event for deep inelastic electron-photon scattering is discouraged by the authors [15], but the effect of the underlying event was considered in estimating the systematic error on F_2^γ as detailed in section 6.3.

F2GEN assumes a two-quark state in the $\gamma^\star\gamma$ centre-of-mass system and uses the JETSET string fragmentation algorithm to convert it to hadrons. The angular distribution of the two outgoing quarks in the $\gamma^\star\gamma$ centre-of-mass system is chosen either to be "pointlike" or "peripheral". Pointlike here means that the angular distribution is the same as it would be for lepton pair production from two real photons, as if no hard final state QCD radiation occurred and as if photons had no hadron-like component – clearly an unphysically extreme case, but interesting for comparison with other models. Peripheral means that the angle between the outgoing quarks and the incoming photons in the centre-of-mass system is randomly sampled so as to give an exponential distribution of transverse momentum with a mean of 300 MeV, as if all the photons interacted as pre-existing hadrons and direct photon-quark coupling never occurred – another unphysically extreme case. In previous OPAL analyses the pointlike prescription was used for a sample of events generated with the FKP structure function [5] and added to a peripheral sample generated with a Vector Meson Dominance structure function [6]. It is now acknowledged that the FKP structure function is not likely to be reliable for $x < 0.1$ [24]; see Ref. [25] for a detailed discussion.

Other parametrisations of F_2^γ, such as the one based on the leading order (LO)

GRV [26], and SaS1D [25] parton density functions (PDFs) used in this analysis, are defined so as to include both the direct photon-quark coupling and the effect of the hadronic part of the photon. At low x it is expected that the hadronic part dominates.

In order to take this into account, some of the F2GEN samples have been produced with the so-called "perimiss" combination. For x values less then $x_{cut} = 0.05$, all events generated with the given structure function are given the peripheral angular distribution. Above x_{cut} they are picked by a hit-or-miss Monte Carlo choice to come from either a pointlike or a peripheral sample, according to the ratio of the VDM F_2^γ to the total F_2^γ at that x and Q^2 for a given PDF (more details in Ref. [27]).

The various options discussed above make it possible to investigate the dependence of the measured F_2^γ on the modelling of the hadronic final state in more detail than was possible in earlier investigations.

The contribution to F_2^γ from the charm quark is treated differently in different samples. F2GEN (pointlike or perimiss) uses F_2^γ for three light flavours (u, d, s) with an extra QPM charm sample added using the Vermaseren program. The SaS1D and the GRV parametrisations of the PDFs treat charm as a Bethe-Heitler contribution to F_2^γ which is taken into account if W exceeds twice the mass of the charm quark ($W > 2m_c$), where m_c is taken to be 1.3 GeV and 1.5 GeV in the two parametrisations, respectively. In contrast, in the version of the GRV parametrisation which was used for the event generation of the HERWIG samples – the GRV parametrisation in the form available from the PDFLIB library [28] – charm is treated as a massless quark which contributes to F_2^γ, independently of W for $Q > 2m_c$. Also, the Monte Carlo programs themselves contain different assumptions for m_c (1.6 GeV in the Vermaseren program, 1.8 GeV in HERWIG, and 1.35 GeV in PYTHIA). During event generation in HERWIG the contribution of charm to F_2^γ is neglected for $W < 2m_c$, independently of the particular parametrisation of the parton density functions used. This has been taken into account when deriving F_2^γ.

The background to the $\gamma^\star\gamma \to$ hadrons signal comes from events which contain a true or fake tagged electron and an apparent low-mass hadronic final state (compared to the e^+e^- centre-of-mass energy). The dominant background sources are $\gamma^\star\gamma \to \tau^+\tau^-$ and $Z^0 \to$ hadrons events. They have been simulated with the Vermaseren program for $\gamma^\star\gamma \to \tau^+\tau^-$ and with the JETSET Monte Carlo for $Z^0 \to$ hadrons. Additional background sources are four-fermion events with $e^+e^- q\overline{q}$ and $e^+e^- \tau^+\tau^-$ final states, and $Z^0 \to \tau^+\tau^-$ events. The four-fermion events from the annihilation, bremsstrahlung and conversion diagrams (see Ref. [29] for details) have been simulated by the FERMISV [30] and PYTHIA programs, and the $Z^0 \to \tau^+\tau^-$ events by the KORALZ generator [31]. The sum of these contributions is estimated to be of the order of 1 to 2% for each of the two samples. After applying the cuts as defined in section 3 for the low-Q^2 and high-Q^2 samples the total background is approximately 9% and 12% in the two samples, respectively. The number of selected events in the data and the expected contributions of background events from the main sources are listed in table 2, where

the quoted errors are statistical only.

sample	selected	$\gamma^\star\gamma \to \tau^+\tau^-$	$Z^0 \to$ hadrons
low-Q^2	5455	289.4 ± 12.7	122.0 ± 12.0
high-Q^2	225	18.5 ± 3.3	3.5 ± 2.0

Table 2: The number of selected events in the data, and the expected dominant background contributions obtained from the Monte Carlo models, normalised to the data luminosity, in the low-Q^2 and high-Q^2 samples, respectively.

5 Data description and modelling of the $\gamma^\star\gamma$ fragmentation

The measurement of F_2^γ and the modelling of the hadronic final state are closely connected, as the measurement of F_2^γ involves the determination of W from the hadronic final state. Because of the finite detector resolution and the incomplete angular coverage the correlation of $W_{\rm vis}$ and W critically depends on the modelling of the hadronic final state. Therefore a detailed comparison of the observed hadronic final state and the predictions from the various Monte Carlo models is necessary. The results of this study are summarised in this section.

In former analyses final state hadrons going into the forward region of the detector were neglected. This was assumed not to cause any problems, for two reasons. Firstly, because at lower centre-of-mass energies the boost in the forward direction was less, so for W greater than 2.5 GeV a larger fraction of the hadrons were seen in the central detectors and were well measured. Secondly, because the simple Monte Carlo models available at that time did not simulate the whole range of possible variations in the $\gamma^\star\gamma$ fragmentation. After the first OPAL analysis of F_2^γ [7] it was realised that this might be an important shortcoming of the commonly used approach [32].

The hadronic system in deep inelastic electron-photon scattering reactions is usually boosted along the beam direction. Figure 2 shows for events selected with the low-Q^2 cuts the prediction from HERWIG for the hadronic energy flow per event as a function of the pseudorapidity of the particles. For the purpose of the energy flow analysis a particle is defined as either a track which passes the quality cuts, or an electromagnetic cluster not associated with a track. In all energy flow distributions the tagged electron is not shown. The pseudorapidity is defined as $\eta = -\ln(\tan(\theta'/2))$, where θ' is the polar angle of the particle measured from the direction of the beam that has produced the quasi-real photon, so the tagged electron is at $-3.5 < \eta < -2.8$. This figure demonstrates that, for the selected low-Q^2 singly-tagged sample, a very

significant fraction of the energy flow in events from the HERWIG generator goes into the forward region of the OPAL detector. Two thirds of the energy is deposited in the central region of the detectors, 30% goes into the forward region of the OPAL detector, which in this analysis is defined as the region covered by the FD and SW detectors. As little as 5% of the total hadronic energy is lost in the beampipe. The small inefficiency in the central detector region is mostly due to the fact that some hadrons in this region carry low energy, and therefore fail the track cuts.

The energy in the forward region (25–200 mrad) has been sampled by using the electromagnetic and hadronic energy response of all the OPAL FD and SW detectors with a partial correction for the hadronic energy from charged pions in the FD. About half of the charged pions traverse the electromagnetic detectors without depositing energy above the threshold of 2 GeV. About 42% of the total hadronic energy in the forward region can be recovered, with an energy resolution of $\Delta E/E = 30\%$ of the seen energy.

The visible invariant mass $W_{\rm vis}$ of the hadronic event is obtained from the four-momenta of all visible particles in the event, apart from the tagged electron. Then $x_{\rm vis}$ is calculated from $W_{\rm vis}$ and Q^2 using Eq. 3. As a result of including the forward region, the correlation between W and $W_{\rm vis}$ at large W is substantially increased. Figure 3 (a) shows the correlation of W and $W_{\rm vis}$ for the HERWIG Monte Carlo with and without the use of the forward region of the OPAL detector, emphasising the importance of the energy measurement in this region. The degree of correlation between $W_{\rm vis}$ and W also depends on the Monte Carlo model used. The pointlike sample from F2GEN (figure 3 (b)) maintains the correlation up to higher values of W than the HERWIG sample, and with the addition of forward energy the correlation becomes even better.

The Monte Carlo models describe many of the data distributions reasonably well. Figure 4 shows some examples before the subtraction of background events. In the distribution of the energy of the tagged electron in figure 4 (a) the background from $\rm Z^0 \rightarrow$ hadrons is clearly visible peaking at a low fraction of the beam energy. Most of this background is removed by requiring $E_{\rm tag} > 0.775\, E_{\rm b}$ (indicated by the vertical line; see section 3). The background is shown at the bottom of the plots and has been added to the HERWIG and PYTHIA samples which have been normalised to the luminosity of the data. The differences at low $\theta_{\rm tag}$ in figure 4 (b) are due to the installation of the small angle luminometer part of the way through the data taking (see section 2). The Monte Carlo samples shown here do not account for the period before the installation. A cut at $\theta_{\rm tag} > 60$ mrad removes this region.

Figure 5 (a) shows that both HERWIG and PYTHIA are in reasonable agreement with the $W_{\rm vis}$ distribution measured in the data in the low-Q^2 sample, at least for $W_{\rm vis} < 20$ GeV. Figures 5 (b)–(d) demonstrate that none of the generators represents the final state accurately. While the distribution of the transverse momentum $p_{\rm t,in}$ in the tag plane (defined by the beam direction and the direction of the tagged electron) shows only moderate discrepancies, quantities such as the total visible energy $E_{\rm vis}$ in

the event, or the transverse energy $E_{\mathrm{t,out}}$ out of the tag plane, show clear discrepancies between models and data. It is clear from figure 5 (d) in particular that the data extend into regions of phase space which PYTHIA does not populate at all. Figure 6 shows the same distributions for the high-Q^2 sample. This region is less dependent on the modelling of the non-perturbative component. As a consequence, the overall agreement between data and Monte Carlo models is better for this sample.

The failure of the models in the low-Q^2 region is most marked at low x_{vis} as figure 7 illustrates. This figure shows the $E_{\mathrm{t,out}}$ distributions in three x_{vis} ranges. For $x_{\mathrm{vis}} > 0.1$, all of the generators are adequate, but for $x_{\mathrm{vis}} < 0.1$ the generators are mutually inconsistent, and in disagreement with the data. At high $E_{\mathrm{t,out}}$ the data show a clear excess over HERWIG and PYTHIA, while the pointlike F2GEN sample exceeds the data in the region of high $E_{\mathrm{t,out}}$.

The differences between Monte Carlo models and data in the low-Q^2 region become even more apparent when the energy flow per event is plotted as a function of pseudorapidity and the azimuthal angle $\Delta\phi$, where $\Delta\phi = \phi - \phi_{tag}$. Figure 8 shows the energy flow per event for the data and three Monte Carlo models. Most hadronic energy is clustered around $\Delta\phi = \pi$, balancing the transverse momentum of the tagged electron with respect to the beam. While, around $\Delta\phi = \pi$, HERWIG shows a concentration of energy flow in the hemisphere which contains the tagged electron, the data and the F2GEN pointlike sample project more of the hadronic energy into the other hemisphere. Figure 9 shows the same energy flow per event as a function of pseudorapidity only, summing over all $\Delta\phi$. The energy flow is plotted in bins of x_{vis} and θ_{tag}. The two regions in θ_{tag} correspond to an average squared momentum transfer of $\langle Q^2 \rangle = 8.5$ GeV^2 and $\langle Q^2 \rangle = 16.5$ GeV^2. As was observed in figure 7, the largest differences between the data and Monte Carlo distributions appear at $x_{\mathrm{vis}} < 0.1$. Both HERWIG and PYTHIA have an excess of energy close to $\eta \simeq -1$ in the hemisphere which contains the tagged electron. While both underestimate the energy projected in the pseudorapidity region of $1.5 < \eta < 2$, they seem to generate too much energy in the forward region of $\eta > 2.3$. The pointlike events of the F2GEN sample, on the other hand, overestimate the energy flow, in particular for $x_{\mathrm{vis}} < 0.1$, but tend to model the peak in the data better at $1.5 < \eta < 2$ and $\theta_{\mathrm{tag}} > 75$ mrad.

Based on the detection efficiency of the OPAL detector modelled by the simulation program [20] the energy flow of the data was corrected in each bin of pseudorapidity and compared directly with the generated energy of each Monte Carlo model. The results are shown in figure 10 for the low-Q^2 region and in figure 11 for the high-Q^2 region. The event selection cuts, as described in section 3, have been applied to these distributions. The correction factors for the data were computed by dividing the histogram of the energy flow at the generator level by the corresponding histogram after detector simulation, such as shown in figure 2. These correction factors obtained from the different Monte Carlo models were averaged, and the difference between the models is taken as the systematic error.

The serious discrepancies between the data and any of the available Monte Carlo models are seen both within the central region of the detector ($|\eta| < 2.3$), where the energy flow is well measured, and in the forward region, where the energy can only be sampled. Figure 10 shows that the pointlike and HERWIG Monte Carlo samples differ from one another as markedly in the forward region as they do in the central detector region. The fact that the PYTHIA and HERWIG simulations agree quite well with each other in the forward region cannot be taken as reassuring, since they both disagree with the data very clearly. In the forward region the data points in figure 10 lie closer to the pointlike simulation than to HERWIG or PYTHIA. It is from this region of acceptance that the largest uncertainties arise in the measurement of W and hence of x. Overall the energy flow at high Q^2, figure 11, appears to be better modelled by all generators, but the energy flow in the forward region is still overestimated by HERWIG and PYTHIA. The difference between the pointlike and perimiss samples from F2GEN is much reduced compared to figure 10.

It is clear from the figures 8–11 that the unfolding will have large errors as long as the energy flow from the different models remains in clear disagreement with the energy flow in the data, in particular in the region of $x_{\rm vis} < 0.1$ and $Q^2 < 30$ GeV^2. This problem needs to be addressed in the framework of the models, in order significantly to reduce the systematic error. The distribution in figure 10 for the perimiss version of F2GEN (see definition in section 4 above) is very similar in character to those for the QCD motivated models, HERWIG and PYTHIA. But there is only one difference between the two F2GEN samples; the angular distribution of the outgoing quarks in the $\gamma^\star\gamma$ centre-of-mass system. At $\eta > 2$ the data are much closer to the pointlike distribution than to perimiss or the QCD models. This indicates that in tuning these models particular attention will need to be given to the angular distributions of partons in the $\gamma^\star\gamma$ system.

6 The determination of F_2^γ

It has been shown that the generators give an adequate description of the hadronic system for $x_{\rm vis} > 0.1$, although significant discrepancies are seen at lower $x_{\rm vis}$. With this limitation in mind, F_2^γ has been determined as a function of x in bins of Q^2 from the $x_{\rm vis}$ distribution using the method of regularised unfolding [33]. The measurement presented here is mainly based on the HERWIG Monte Carlo model. The PYTHIA and the F2GEN models are used to estimate the model dependence of the result.

6.1 General considerations

The principle of the unfolding is the following. The distribution $g^{\rm det}$ of a quantity u (e.g. $x_{\rm vis}$) directly measured by the detector is related to the distribution $f^{\rm part}$ of a

partonic variable ω (e.g. x) by an integral equation which expresses the convolution of the true distribution with all effects that occur between the creation of the hard process and the measurement $g^{\rm det}(u) = \int A(u,\omega)\, f^{\rm part}(\omega)\, d\omega + B(u)$, where $B(u)$ represents an additional contribution from background events. This integral equation is transformed into a matrix equation, and solved numerically, leading to the histogram $f^{\rm part}(\omega)$. This simple method can produce spurious oscillating components in the result due to limited detector resolution and statistical fluctuations. Therefore the method has to be improved by a regularisation procedure which reduces these oscillations.

Technically, in the analysis performed here, the unfolding works as follows. A set of Monte Carlo events is used as an input to the unfolding program [34]. These events are based on an input F_2^γ and implicitly carry the information about the response function $A(x_{\rm vis}, x)$. A continuous weight function $f_{\rm mult}(x)$ is defined which depends only on x. This function is used to calculate an individual weight factor for each Monte Carlo event. The weight function is obtained by a fit of the $x_{\rm vis}$ distribution of the Monte Carlo sample to the measured $x_{\rm vis}$ distribution of the data, such that the reweighted Monte Carlo events describe as well as possible the $x_{\rm vis}$ distribution of the data. After the unfolding both distributions agree with each other on a statistical basis. The unfolded $F_2^\gamma(x, Q^2)$ from the data is then obtained by multiplying the input $F_2^\gamma(x, Q^2)$ of the Monte Carlo with the weight function $f_{\rm mult}(x)$.

The data were subdivided into three ranges of Q^2, two ranges for the low-Q^2 sample and one for the high-Q^2 sample, with approximate ranges of 6–8, 8–30 and 60–400 GeV^2 and with average squared momentum transfers $\langle Q^2 \rangle =$ 7.5, 14.7 and 135 GeV^2. The $x_{\rm vis}$ distributions for the three data sets are shown in figure 12 (a)–(c); the symbols used here also apply to figures 13 and 14. The distributions of the signal Monte Carlo (HERWIG using the GRV parametrisation) with the background added to it are shown as the dashed histogram. In addition the background events are shown separately at the bottom of the figure. The numbers of Monte Carlo events in each bin are absolute predictions calculated for the data luminosity. The result of the unfolding is shown as the open histogram, which represents the signal Monte Carlo with the background added to it after the unfolding has been performed. It is observed that the mean $x_{\rm vis}$ increases with increasing Q^2, and that the $x_{\rm vis}$ distribution of the data is well represented by the sum of the signal and background Monte Carlo samples after unfolding. On average, in order to fit the measured $x_{\rm vis}$ distribution, the unfolding has increased the weights of the Monte Carlo events. The total change amounts to 8%, 15%, 6%, for $\langle Q^2 \rangle =$ 7.5, 14.7 and 135 GeV^2, respectively. It can also be seen from figure 12 that not only the total number of events, but also the shape of the $x_{\rm vis}$ distribution, is slightly changed by the unfolding.

6.2 Checks of the unfolding procedure

The unfolding procedure delivers a weight for each Monte Carlo event as described above, which can then be used to reweight the Monte Carlo distributions of different

variables. Any reweighting based on the generated x distribution will change the shape of other measurable variables besides $x_{\rm vis}$. Therefore the comparison of these distributions with the data gives an important check of the transformation, as described by the Monte Carlo simulation, between the partonic distributions and the measurable distributions.

Figures 13 and 14 show examples of those distributions, applying the cuts as listed in section 3. Different distributions are chosen in figures 13 and 14 in order to display a larger set of variables. Figure 13 compares the data and the HERWIG Monte Carlo at $\langle Q^2 \rangle = 14.7$ GeV^2. The distributions shown are (a) the energy of the tagged electron $E_{\rm tag}$ as a fraction of the beam energy $E_{\rm b}$, (b) the polar angle $\theta_{\rm tag}$ of the tagged electron, (c) the visible invariant mass $W_{\rm vis}$ of the hadronic system, and (d) the number of charged particles $N_{\rm ch}$ seen in the detector. Figure 14 shows a similar comparison of the PYTHIA Monte Carlo sample with the data at $\langle Q^2 \rangle = 135$ GeV^2. The variables shown are (a) $E_{\rm tag}/E_{\rm b}$, (b) the measured Q^2, (c) the neutral energy $E_{\rm neut}$, which is obtained by adding up the energy of the calorimeter clusters which cannot be associated with tracks, and (d) the missing longitudinal momentum of the event scaled by the beam energy. The distributions from both Monte Carlo samples are slightly lower than the distributions observed in the data, both for the quantities measured from the electron and for distributions obtained from the hadronic final state, and the agreement improves significantly after the reweighting based on the unfolding of the $x_{\rm vis}$ distribution.

The impact of different parton density parametrisations and fragmentation models on the unfolded result has been assessed by applying the unfolding procedure to several samples of Monte Carlo events. Figure 15 shows some examples for two mock data samples; in each case the unfolding Monte Carlo was HERWIG with the GRV parametrisation. The mean value of F_2^γ in each bin as assumed in the unfolding Monte Carlo is shown as the solid lines.

In figure 15 (a), (b) HERWIG Monte Carlo events with SaS1D are used as mock data. The unfolding should recover the F_2^γ based on the SaS1D parametrisation, which is represented by the mean value of F_2^γ in each bin shown as the dash-dotted lines. The charm threshold as assumed in HERWIG, which leads to an abrupt drop of the parametrisation at medium x (at 0.37 for (a) and 0.53 for (b)), lies within the range studied, and is taken into account in the evaluation of the mean values. The trend of the distribution is recovered, but at small values of x the result falls too low, and at large values of x the result is much higher than the F_2^γ based on the SaS1D parametrisation.

In figure 15 (c), (d) the mock data were generated using PYTHIA, again with the SaS1D PDF. This check mainly shows the effect of the different $\gamma^\star\gamma$ fragmentation as implemented in HERWIG and PYTHIA. The unfolding result of the three lowest points in figure 15 (c) is about right, whereas the point at high x is much too low. This effect, which is even more dramatic in figure 15 (d), is not yet fully understood. It is assumed to arise from the difference in the generators at low W and correspondingly

large x, which means at low energies of the quasi-real photon (see section 4).

In the unfolding of the data all the different Monte Carlo samples are used (see section 6.3). The systematic effects observed in the different Monte Carlo samples are included in the evaluation of the systematic errors of the unfolding result. The total error is dominated by this contribution.

6.3 Results

In order to measure the central values of F_2^γ in bins of x a "reference" unfolding is defined. It is based on a HERWIG Monte Carlo sample, which uses the GRV parametrisation and no soft underlying event. The event selection cuts as described in section 3 are applied.

Each Q^2 range is unfolded separately, with the x binning chosen as in a former analysis [7], to allow for a direct comparison. The unfolded F_2^γ measurements are shown in figure 16 (a)–(c), and listed in table 3. The figures also show the F_2^γ calculated from the GRV and the SaS1D parton density parametrisation, both using the charm contribution to F_2^γ for massive charm quarks and both evaluated at the corresponding $\langle Q^2 \rangle$ values. The value of F_2^γ/α is given at the centre of the x bin. The bin sizes

$\langle Q^2 \rangle$	Bin	x	F_2^γ/α
7.5 GeV^2	I	$0.001 < x < 0.091$	$0.28 \pm 0.02 \,^{+0.03}_{-0.10}$
	II	$0.091 < x < 0.283$	$0.32 \pm 0.02 \,^{+0.08}_{-0.13}$
	III	$0.283 < x < 0.649$	$0.38 \pm 0.04 \,^{+0.06}_{-0.21}$
14.7 GeV^2	I	$0.006 < x < 0.137$	$0.38 \pm 0.01 \,^{+0.06}_{-0.13}$
	II	$0.137 < x < 0.324$	$0.41 \pm 0.02 \,^{+0.06}_{-0.03}$
	III	$0.324 < x < 0.522$	$0.41 \pm 0.03 \,^{+0.08}_{-0.11}$
	IV	$0.522 < x < 0.836$	$0.54 \pm 0.05 \,^{+0.31}_{-0.13}$
135 GeV^2	I	$0.100 < x < 0.300$	$0.65 \pm 0.09 \,^{+0.33}_{-0.06}$
	II	$0.300 < x < 0.600$	$0.73 \pm 0.08 \,^{+0.04}_{-0.08}$
	III	$0.600 < x < 0.800$	$0.72 \pm 0.10 \,^{+0.81}_{-0.07}$

Table 3: Results for F_2^γ as a function of x for four active flavours in bins of Q^2. The first errors are statistical and the second systematic. See text for details.

are indicated by the vertical lines at the top of the figure. The vertical error bars show both the statistical error alone and the full error, given by the quadratic sum of statistical and systematic errors. The central values and statistical errors of the F_2^γ

measurements were estimated using the reference unfolding.

The estimation of the systematic error includes three parts: the variation of the compositions of signal and background events in the sample, the use of different F_2^γ structure functions assumed in the Monte Carlo samples, and the different modelling of the formation of the hadronic final state.

In order to allow for varying compositions of signal and background events, the event selection cuts were varied as listed in table 4. The choice of the cut variations reflects the different population of signal events in the three Q^2 ranges, in terms of the scattering angle of the electron and $W_{\rm vis}$, as well as the different behaviour of the background events. The unfolding was carried out using HERWIG with the GRV parametrisation and only one cut (e.g. a lower or upper restriction in $W_{\rm vis}$) was varied from the standard set in each unfolding. To study the uncertainty due to the structure

	$\langle Q^2 \rangle = 7.5$ GeV^2	$\langle Q^2 \rangle = 14.7$ GeV^2	$\langle Q^2 \rangle = 135$ GeV^2
min $E_{\rm tag}$	$E_{\rm tag} > 0.70,\ 0.85\,E_{\rm b}$	$E_{\rm tag} > 0.70,\ 0.85\,E_{\rm b}$	$E_{\rm tag} > 0.85\,E_{\rm b}$
min $\theta_{\rm tag}$ [mrad]	$\theta_{\rm tag} > 65$	$\theta_{\rm tag} > 70$	$\theta_{\rm tag} > 250$
max $\theta_{\rm tag}$ [mrad]	–	$\theta_{\rm tag} < 110$	$\theta_{\rm tag} > 380$
min $W^2_{\rm vis}$ [GeV^2]	$W^2_{\rm vis} > 10$	$W^2_{\rm vis} > 10$	$W^2_{\rm vis} > 20,\ 100$
max $W^2_{\rm vis}$ [GeV^2]	$W^2_{\rm vis} < 400$	$W^2_{\rm vis} < 400$	$W^2_{\rm vis} < 400,\ 800$
$p_{\rm t}$ [GeV]	$p_{\rm t,out} < 6$ and $p_{\rm t,bal} < 4$	$p_{\rm t,out} < 6$ and $p_{\rm t,bal} < 4$	–
antitag	–	–	$E_{\rm a} < 0.2\,E_{\rm b}$

Table 4: The list of variations of the kinematical cuts. A dash means that no variation was performed.

functions assumed in the Monte Carlo samples, for the low-Q^2 sample, the unfolding was done using the HERWIG generator, the standard set of cuts and the SaS1D PDF's. The effect of the different modelling of the formation of the hadronic final state was studied in two ways. The unfolding was repeated for the low-Q^2 sample using HERWIG with the standard cuts but simulating the soft underlying event (SUE). To evaluate the dependence on the chosen Monte Carlo model (HERWIG, PYTHIA or F2GEN) the unfolding was done for the standard cuts but either using PYTHIA with the SaS1D parametrisation, or using F2GEN as explained below. The difference between these results and the reference unfolding is quoted as the model dependence. A summary of the observed differences between the various unfolding result and the central value can be found in table 5. The quoted values are the maximum deviations in each category from the result of the reference unfolding on both sides. If the variation is to one side, only one value is quoted. The systematic error assigned to the result, shown in table 3,

is taken as the maximum deviation from the central value.

	$\langle Q^2 \rangle = 7.5$ GeV^2			$\langle Q^2 \rangle = 14.7$ GeV^2			
Bin	I	II	III	I	II	III	IV
E_{tag}	-0.01	$^{+0.04}_{-0.03}$	$^{+0.01}_{-0.02}$	$^{+0.02}_{-0.01}$	$^{+0.01}_{-0.02}$	$^{+0.02}_{-0.02}$	$^{+0.02}_{-0.01}$
θ_{tag}	$+0.03$	-0.13	-0.08	< 0.01	-0.02	$+0.04$	$^{<+0.01}_{-0.10}$
W^2_{vis}	$^{<+0.01}_{-0.01}$	-0.02	$^{+0.01}_{<-0.01}$	< 0.01	-0.02	$+0.05$	-0.12
p_{t}	-0.01	< 0.01	$+0.01$	< 0.01	< 0.01	< 0.01	< 0.01
PDF	$+0.03$	< 0.01	-0.21	$+0.06$	$+0.02$	-0.11	-0.13
SUE	-0.04	-0.09	$+0.05$	-0.05	-0.03	< 0.01	$+0.02$
model	$^{+0.01}_{-0.10}$	$^{+0.08}_{-0.02}$	$^{+0.06}_{-0.06}$	$^{+0.03}_{-0.13}$	$+0.06$	$^{+0.08}_{-0.03}$	$+0.31$

	$\langle Q^2 \rangle = 135$ GeV^2		
Bin	I	II	III
E_{tag}	$+0.07$	$^{+0.04}_{-0.03}$	-0.07
θ_{tag}	$+0.33$	$^{+0.01}_{-0.08}$	$+0.11$
W^2_{vis}	$^{+0.02}_{-0.03}$	$^{+0.01}_{-0.06}$	$^{+0.26}_{<-0.01}$
antitag	-0.01	< 0.01	-0.02
model	$^{+0.04}_{-0.06}$	$^{+0.03}_{-0.04}$	$+0.81$

Table 5: The differences between the various unfolding results and the result of the reference unfolding for F_2^γ for four active flavours as a function of x in bins of Q^2. SUE denotes the soft underlying event explained in the text. The bins are defined in table 3.

Since with F2GEN only light quarks (u, d, s) were generated for both Q^2 samples, F2GEN can be used only to evaluate F_2^γ for three active flavours; therefore the systematic uncertainty due to the use of F2GEN was treated differently. It was verified that the contributions of charm to F_2^γ from the HERWIG and Vermaseren programs agree with each other. The charm contribution as predicted by the Vermaseren program was subtracted from the data leading to a data sample corresponding to an F_2^γ with three active flavours. This data sample was then unfolded using the F2GEN generator assuming the hadronic final state to be entirely pointlike or using the perimiss option explained in section 4, and with the HERWIG model based on four active flavours, all leading to a three flavour result for the unfolded F_2^γ from the data. In some of the bins, especially at low x and Q^2, the difference in the results for the three flavour F_2^γ of HERWIG and F2GEN is the largest uncertainty. This difference scaled by the ratio of the HERWIG four flavour and three flavour results was included in the evaluation of the the model dependence in table 5.

Taking into account all effects studied above the systematic errors are considerably larger than evaluated in the old style determinations of F_2^γ, such as e.g. in Ref. [7]. The unfolded results on F_2^γ as a function of x are well described by the F_2^γ structure functions obtained from the GRV and SaS1D parton density parametrisations in all Q^2 ranges.

Because of the systematic limitations in the regimes of low and high x, discussed in section 5 and section 6.2, the measurement of F_2^γ/α as a function of Q^2 is restricted to the less problematic region of mean x values $0.1 < x < 0.6$ where, as can be seen from figure 12, data at all $\langle Q^2 \rangle$ are available. The result is shown in figure 16 (d) and listed in table 6. A clear increase of F_2^γ/α with Q^2 is observed in the data, in agreement with the QCD prediction. For this result the systematic error is evaluated in the same way

$\langle Q^2 \rangle$	7.5 GeV^2	14.7 GeV^2	135 GeV^2
F_2^γ/α	$0.36 \pm 0.02 \,^{+\,0.06}_{-\,0.12}$	$0.41 \pm 0.01 \,^{+\,0.08}_{-\,0.04}$	$0.71 \pm 0.07 \,^{+\,0.14}_{-\,0.05}$

Table 6: Results for F_2^γ for four active flavours averaged over $0.1 \leq x \leq 0.6$ in bins of Q^2. The first errors are statistical and the second systematic. See text for details.

as stated above. Table 7 shows a list of the components contributing to the systematic uncertainty.

	$\langle Q^2 \rangle = 7.5$ GeV^2	$\langle Q^2 \rangle = 14.7$ GeV^2	$\langle Q^2 \rangle = 135$ GeV^2
E_{tag}	$^{+\,0.02}_{-\,0.02}$	$^{+\,0.01}_{<-\,0.01}$	$^{+\,0.07}_{-\,0.01}$
θ_{tag}	-0.10	$^{+\,0.01}_{-\,0.01}$	$+0.135$
W^2_{vis}	$^{+\,0.01}_{<-\,0.01}$	$+0.02$	$^{<+\,0.01}_{-\,0.02}$
p_{t}	< 0.01	< 0.01	–
antitag	–	–	-0.01
PDF	-0.12	-0.04	–
SUE	-0.01	-0.03	–
model	$^{+\,0.06}_{-\,0.02}$	$+0.08$	$^{+\,0.01}_{-\,0.05}$

Table 7: The differences between the various unfolding results and the result of the reference unfolding for F_2^γ for four active flavours averaged over $0.1 \leq x \leq 0.6$ in bins of Q^2. For explanations see table 5.

The measurement of the slope $\mathrm{d}(F_2^\gamma/\alpha)/\mathrm{d}\ln Q^2$ is a basic test of QCD, which has been carried out at lower centre-of-mass energies. A summary of the results can be found in Ref. [4]. At a finite value of Q^2 the structure function F_2^γ is predicted by the

inhomogenous Altarelli–Parisi evolution equations [35] depending on a specific ansatz for F_2^γ at a low scale $Q_0^2 < Q^2$. The specific ansatz divides the structure function F_2^γ at Q_0^2 with some arbitrariness into two parts, the hadronic part, and the pointlike part. The hadronic part is a non-perturbative input and it is usually parametrised as a function of x. Commonly used parametrisations are $F_{2,\mathrm{had}}^\gamma/\alpha = 0.2(1-x)$ or $F_{2,\mathrm{had}}^\gamma/\alpha = 0.2\,x^{0.4}(1-x)$ [4]. The asymptotic limit $Q^2 \to \infty$ [36] of the pointlike part is calculable in perturbative QCD. In the leading logarithmic approximation it is $F_{2,\mathrm{pl}}^\gamma/\alpha = \frac{3}{\pi}\sum_f \mathrm{e}_\mathrm{q}^4 \cdot x \cdot (x^2 + (1-x)^2) \ln \frac{Q^2}{\mu^2}$. Here μ^2 is a parameter of the order of the QCD scale parameter Λ_{QCD}. The sum over all quark charges e_q runs over all active flavours f. Although at finite values of Q^2 the asymptotic solution is not applicable, the $\ln Q^2$ behaviour of the pointlike part and therefore of F_2^γ is retained.

Based on this observation a first simple attempt to measure $\mathrm{d}(F_2^\gamma/\alpha)/\mathrm{d}\ln Q^2$ at LEP was made by fitting a linear function of the form $a + b \ln \frac{Q^2}{\mathrm{GeV}^2}$ to the three data points in figure 16, where a and b are parameters which do not depend on x. This approach does not take into account effects due to the charm threshold which lies within the range in x used for the two lowest points, and varies from point to point. Also no assumptions are made on the x dependence of the hadronic part of F_2^γ. The fit was performed using the measured values and errors listed in table 6 and assuming the errors to be uncorrelated. Taking the total errors on F_2^γ the result is

$$F_2^\gamma(Q^2)/\alpha = (0.08^{+\,0.13}_{-\,0.18}) + (0.13^{+\,0.06}_{-\,0.04}) \ln \frac{Q^2}{\mathrm{GeV}^2}\,,$$

with $\chi^2/\mathrm{dof} = 0.05$ (correlation coefficient -0.95 between the two parameters). The errors and the correlation of the parameters are as given by MINUIT [37]. The slope $\mathrm{d}(F_2^\gamma/\alpha)/\mathrm{d}\ln Q^2$ is significantly different from zero. The low value of χ^2/dof indicates that the errors are estimated generously. In order to make a more precise measurement of $\mathrm{d}(F_2^\gamma/\alpha)/\mathrm{d}\ln Q^2$ the error determination has to be addressed and a more elaborate procedure, taking possible correlations between the data at different $\langle Q^2 \rangle$ into account, has to be applied in the future. The results using statistical errors only are $a = 0.11 \pm 0.06$ and $b = 0.11 \pm 0.02$ with $\chi^2/\mathrm{dof} = 1.05$ (the two parameters have a correlation coefficient of -0.99).

In figure 16 (d) the data are compared to several theoretical calculations. As in figure 16 (a)–(c) the LO predictions of the GRV parametrisation and the SaS1D parametrisation having a contribution to F_2^γ from massive charm quarks are shown. The curve labeled HO [38] is a higher order (HO) prediction based on the HO GRV parametrisation for three light quarks, complemented by the contribution of charm quarks to F_2^γ based on the HO calculation using massive charm quarks of Ref [39]. In this prediction the three light flavours are decoupled from the charm quarks in the evolution of F_2^γ. The QCD scale parameter $\Lambda_3^{\overline{\mathrm{MS}}}$ for three flavours was taken to be 248 MeV. The renormalisation and factorisation scale are assumed to be Q^2, and the mass of the charm quark is 1.5 GeV. The difference between the HO prediction and the LO predictions is rather small. The predicted values of $\mathrm{d}(F_2^\gamma/\alpha)/\mathrm{d}\ln Q^2$ are 0.100 for GRV

(LO) and SaS1D (LO) and 0.105 for the higher order calculation. The HO result is also quite stable against scale variations. A change in the renormalisation scale and factorisation scale from Q^2 to $Q^2/4$ and $4Q^2$ results in a change in $\mathrm{d}(F_2^\gamma/\alpha)/\mathrm{d}\ln Q^2$ of less than 1% compared to the result when Q^2 is taken as the scale. The theoretical uncertainty is much smaller than the experimental one, and it is very desirable to reduce the systematic uncertainty of the measurement in the future.

The F_2^γ values presented here are not corrected for the effect of nonzero virtuality P^2 of the quasi-real photon. The P^2 allowed by the antitag condition for an electron at the lower edge of the angular acceptance of the detector is 0.33 GeV^2 and 0.20 GeV^2 for the low-Q^2 and high-Q^2 samples, respectively. The mean values of the virtuality of the quasi-real photon, $\langle P^2 \rangle$, as predicted by the HERWIG and F2GEN models are shown in table 8. The numbers give the predicted range of values depending on the PDF and $\gamma^\star\gamma$ fragmentation chosen within the models. Sizable differences in the predictions are observed. There exist several theoretical ansatzes of how F_2^γ should

	$\langle P^2 \rangle$	
	low-Q^2	high-Q^2
HERWIG	0.06 – 0.09 GeV^2	0.03 – 0.05 GeV^2
F2GEN	0.20 – 0.50 GeV^2	0.05 – 0.08 GeV^2

Table 8: Ranges of the predictions of $\langle P^2 \rangle$ of the Monte Carlo models for the two samples.

behave as a function of P^2 [40–42]. Based on the P^2 dependent version of the SaS1D parametrisation the effect on $F_2^\gamma(x, Q^2, P^2)$ was studied using as P^2 the mean values predicted by the HERWIG model (see table 8) and the recommended scheme of Ref. [41] to evaluate the off-shell anomalous component for low P^2. As an example the results for two particular x values (see table 3) and for $Q^2 = 14.7$ GeV^2 are listed in table 9. A strong drop of $F_2^\gamma(x, Q^2, P^2)$ with P^2 is observed, which also changes with x. As the distribution of P^2 in the data and the correct theoretical prescription are not known, no correction is applied.

	$x = 0.006$		$x = 0.522$	
P^2	0.06 GeV^2	0.09 GeV^2	0.06 GeV^2	0.09 GeV^2
$1 - \dfrac{F_2^\gamma(x, Q^2, P^2 \neq 0)}{F_2^\gamma(x, Q^2, P^2 = 0)}$	21%	29%	5.4%	8.6%

Table 9: The dependence of $F_2^\gamma(x, Q^2, P^2)$ on P^2 as predicted by the SaS1D parametrisation at $Q^2 = 14.7$ GeV^2 for different values of x.

7 Summary and conclusions

The full data sample taken by the OPAL experiment at LEP for e^+e^- centre-of-mass energies close to the Z^0 mass has been used to study the properties of hadronic final states in deep inelastic electron-photon scattering, and to determine $F_2^\gamma(x, Q^2)$.

New QCD-based Monte Carlo models (HERWIG 5.8d and PYTHIA 5.718) have become available since the previous OPAL study of such events [7]. The data have been compared with them, for the first time, and with the F2GEN Monte Carlo using two different assumptions on the angular distribution of the hadronic final state. There are significant differences between some aspects of the data and all of the models. The distribution of the energy out of the tag-plane, figure 7, is harder than generated by PYTHIA and HERWIG for measured x values of less than 0.1, and the observed distributions of energy flow per event as a function of pseudorapidity and of azimuthal angle are very different from both HERWIG and PYTHIA (figures 8–10). The distributions for the pointlike F2GEN sample reproduce some parts of the distributions better than either HERWIG or PYTHIA, especially at high pseudorapidity, the region of phase space which is particularly sensitive to the treatment of the hadronic remnant of the quasi-real photon. At central rapidities, however, the data are usually better described by HERWIG and PYTHIA. The data are described reasonably well by the Monte Carlo models for global variables such as the visible hadronic mass, the visible neutral energy, the charged multiplicity, and the energy and scattering angle of the deep inelastic scattered electron (figures 4, 13 and 14).

The photon structure function $F_2^\gamma(x, Q^2)$ has been unfolded as a function of x in three ranges of Q^2. Hadronic energy from the OPAL forward calorimeters has been used in this analysis for the first time, giving a much better correlation, in Monte Carlo studies, between W and the visible mass $W_{\rm vis}$ of the hadronic system. However, for large values of W there are large differences in the degree of correlation between the different Monte Carlo models (figure 3). These differences are closely connected to the differences between the models in the forward energy flow. In order to allow for the uncertainties generated by these differences the full set of Monte Carlo models is used for unfolding, leading to a much increased systematic error on the unfolded F_2^γ.

In this work no attempt has been made to measure F_2^γ at the lowest possible x value by, for instance, unfolding on a logarithmic x scale [43]. This has been driven by the observation of large differences in the energy flow between the data and the different Monte Carlo models, especially at low $x_{\rm vis}$. It will clearly be more difficult to measure F_2^γ at low x in singly-tagged events [27] than had previously been supposed. However, because it has been demonstrated that the energy in the forward region of the detector can be sampled, one can put tighter constraints on the combination of F_2^γ and the $\gamma^*\gamma$ fragmentation, also at low values of x.

The evolution of F_2^γ with Q^2 in the medium x range $0.1 < x < 0.6$ has been measured for mean momentum transfers $\langle Q^2 \rangle = 7.5$, 14.7 and 135 GeV^2. The measurement

shows the logarithmic evolution of F_2^γ with Q^2 expected from QCD. In a rather simple approach, and by using the data from the OPAL experiment alone, a significant rise of F_2^γ with Q^2 was observed. The measured slope is $\mathrm{d}(F_2^\gamma/\alpha)/\mathrm{d}\ln Q^2 = 0.13^{+\,0.06}_{-\,0.04}$, where the error is statistical and systematic. The data, over the x range studied, are equally well described by several of the available parton density parametrisations, including the GRV and SaS1D parametrisations used in this analysis.

Acknowledgements

We thank E. Laenen for providing the higher order calculations and for valuable discussions. We particularly wish to thank the SL Division for the efficient operation of the LEP accelerator and for their continuing close cooperation with our experimental group. In addition to the support staff at our own institutions we are pleased to acknowledge the
Department of Energy, USA,
National Science Foundation, USA,
Particle Physics and Astronomy Research Council, UK,
Natural Sciences and Engineering Research Council, Canada,
Israel Science Foundation, administered by the Israel Academy of Science and Humanities,
Minerva Gesellschaft,
Japanese Ministry of Education, Science and Culture (the Monbusho) and a grant under the Monbusho International Science Research Program,
German Israeli Bi-national Science Foundation (GIF),
Direction des Sciences de la Matière du Commissariat à l'Energie Atomique, France,
Bundesministerium für Bildung, Wissenschaft, Forschung und Technologie, Germany,
National Research Council of Canada,
Hungarian Foundation for Scientific Research, OTKA T-016660, and OTKA F-015089.

References

[1] E. Witten, Nucl. Phys. **B120** (1977) 189;
A. Cordier and P. M. Zerwas, in ECFA Workshop on LEP200, Vol. 1 CERN 87-08, ECFA 87/108, edited by A. Böhm and W. Hoogland, p. 242.

[2] C. F. von Weizsäcker, Z. Phys. **88** (1934) 612;
E. J. Williams, Phys. Rev. **45** (1934) 729.

[3] V. M. Budnev *et al.*, Phys. Rep. **15** (1975) 181.

[4] C. Berger and W. Wagner, Phys. Rep. **146** (1987) 1.

[5] J. H. Field, F. Kapusta and L. Poggioli, Phys. Lett. **B181** (1986) 362;
J. H. Field, F. Kapusta and L. Poggioli, Z. Phys. **C36** (1987) 121;
F. Kapusta, Z. Phys. **C42** (1989) 225.

[6] TPC/2γ Collaboration, H. Aihara *et al.*, Z. Phys. **C34** (1987) 1;
TPC/2γ Collaboration, H. Aihara *et al.*, Phys. Rev. Lett. **58** (1987) 97.

[7] OPAL Collaboration, R. Akers *et al.*, Z. Phys. **C61** (1994) 199.

[8] PLUTO Collaboration, C. Berger *et al.*, Phys. Lett. **B107** (1981) 168;
PLUTO Collaboration, C. Berger *et al.*, Phys. Lett. **B142** (1984) 111;
PLUTO Collaboration, C. Berger *et al.*, Z. Phys. **C26** (1984) 353;
PLUTO Collaboration, C. Berger *et al.*, Nucl. Phys. **B281** (1987) 365.

[9] JADE Collaboration, W. Bartel *et al.*, Z. Phys. **C24** (1984) 231.

[10] TASSO Collaboration, M. Althoff *et al.*, Z. Phys. **C31** (1986) 527.

[11] AMY Collaboration, T. Sasaki *et al.*, Phys. Lett. **B252** (1990) 491;
AMY Collaboration, S. K. Sahu *et al.*, Phys. Lett. **B346** (1995) 208.

[12] TOPAZ Collaboration, K. Muramatsu *et al.*, Phys. Lett. **B332** (1994) 477.

[13] DELPHI Collaboration, P. Abreu *et al.*, Z. Phys. **C69** (1996) 223.

[14] G. Marchesini and B. R. Webber, Nucl. Phys. **B310** (1988) 461;
I. G. Knowles, Nucl. Phys. **B310** (1988) 571;
S. Catani, G. Marchesini and B .R. Webber, Nucl. Phys. **B349** (1991) 635;
G. Abbiendi and L. Stanco, Comp. Phys. Comm. **66** (1991) 16;
G. Abbiendi and L. Stanco, Z. Phys. **C51** (1991) 81;
M. H. Seymour, Z. Phys. **C56** (1992) 161.

[15] M. H. Seymour in L. Lönnblad *et al.*, CERN 96-01 Physics at LEP2, edited by G. Altarelli, T. Sjöstrand and F. Zwirner, (1996) Vol. 2, p. 213;
M. H. Seymour, Proceedings of the Workshop on Two-Photon Physics at LEP and HERA, Lund, May 26-28 1994, edited by G. Jarlskog and L. Jönsson, Lund University, (1994) p. 215.

[16] T. Sjöstrand, Comp. Phys. Comm. **82** (1994) 74;
T. Sjöstrand, PYTHIA 5.7 and JETSET 7.4: Physics and Manual, CERN-TH/93-7112.

[17] T. Sjöstrand in L. Lönblad *et al.*, CERN 96-01 Physics at LEP2, edited by G. Altarelli, T. Sjöstrand and F. Zwirner, (1996) Vol. 2, p. 218.

[18] OPAL Collaboration, K. Ahmet *et al.*, Nucl. Instr. and Meth. **A305** (1991) 275;
P. P. Allport *et al.*, Nucl. Instr. and Meth. **A324** (1993) 34;
P. P. Allport *et al.*, Nucl. Instr. and Meth. **A346** (1994) 476;
B. E. Anderson *et al.*, IEEE Transactions on Nuclear Science **41** (1994) 845.

[19] OPAL Collaboration, G. Alexander *et al.*, Z. Phys. **C52** (1991) 175;
OPAL Collaboration, R. Akers *et al.*, Phys. Lett. **B327** (1994) 397.

[20] J. Allison *et al.*, Nucl. Instr. and Meth. **A317** (1992) 47.

[21] A. Buijs, W. G. J. Langeveld, M. H. Lehto and D. J. Miller, Comp. Phys. Comm. **79** (1994) 523.

[22] J. A. M. Vermaseren, Nucl. Phys. **B229** (1983) 347;
R. Bhattacharya, G. Grammer Jr. and J. Smith, Phys. Rev. **D15** (1977) 3267;
J. Smith, J. A. M. Vermaseren and G. Grammer Jr., Phys. Rev. **D15** (1977) 3280;
J. A. M. Vermaseren, J. Smith and G. Grammer Jr., Phys. Rev. **D19** (1979) 137.

[23] T. Sjöstrand, Comp. Phys. Comm. **39** (1986) 347;
T. Sjöstrand and M. Bengtsson, Comp. Phys. Comm. **43** (1987) 367;
T. Sjöstrand, Comp. Phys. Comm. **82** (1994) 74.

[24] P. Aurenche *et al.*, CERN 96-01 Physics at LEP2, edited by G. Altarelli, T. Sjöstrand and F. Zwirner, (1996) Vol. 1, p. 291;
L. Lönblad *et al.*, CERN 96-01 Physics at LEP2, edited by G. Altarelli, T. Sjöstrand and F. Zwirner, (1996) Vol. 2, p. 187.

[25] G. A. Schuler and T. Sjöstrand, Z. Phys. **C68** (1995) 607.

[26] M. Glück, E. Reya and A. Vogt, Phys. Rev. **D46** (1992) 1973;
M. Glück, E. Reya and A. Vogt, Phys. Rev. **D45** (1992) 3986.

[27] J. J. Ward, PhD Thesis, University College London UCL (1996), unpublished.

[28] H. Plothow-Besch, PDFLIB, User's Manual, CERN Program Library entry W5051
H. Plothow-Besch, Comp. Phys. Comm. **75** (1993) 396.

[29] OPAL Collaboration, G. Alexander *et al.*, Phys. Lett. **B376** (1996) 315.

[30] J. Hilgart, R. Kleiss and F. Le Diberder, Comp. Phys. Comm. **75** (1993) 191.

[31] KORALZ 4.0 Monte Carlo, S. Jadach, B. F. L. Ward and Z. Wąs, Comp. Phys. Comm. **79** (1994) 503.

[32] D. J. Miller, Proceedings of the Workshop on Two-Photon Physics at LEP and HERA, Lund, May 26-28 1994, edited by G. Jarlskog and L. Jönsson, Lund University, (1994) p. 4.

[33] V. Blobel, DESY-84-118, 1984;
V. Blobel, Proceedings of the 1984 CERN School of Computing, Aiguablava, Spain, 9–22 September 1984, CERN 85-09.

[34] V. Blobel, RUN, Regularized Unfolding for High-Energy Physics Experiments, Program manual, (1996), unpublished.

[35] G. Altarelli, G. Parisi, Nucl. Phys. **B126** (1977) 298.

[36] C. Peterson, P. M. Zerwas and T. F. Walsh, Nucl. Phys. **B229** (1983) 301.

[37] F. James and M. Roos, "MINUIT–Function Minimization and Error Analysis", Version 95.03, CERN Program Library D506, CERN, Geneva 1995.

[38] E. Laenen, private communication.

[39] E. Laenen, S. Riemersma, J. Smith and W. L. van Neerven, Phys. Rev. **D49** (1994) 5753.

[40] M. Glück, E. Reya and M. Stratmann, Phys. Rev. **D51** (1995) 3220;
M. Glück, E. Reya and M. Stratmann, DO-TH 96/08, May 1996.

[41] G. A. Schuler and T. Sjöstrand, Phys. Lett. **B376** (1996) 193.

[42] M. Drees and R. M. Godbole, Phys. Rev. **D50** (1994) 3124.

[43] J. J. Ward, Proceedings of the Workshop on Two-Photon Physics from DAΦNE to LEP200 and Beyond, Collège de France, Paris, Feb 2-4 1994, edited by F. Kapusta and J. Parisi, World Scientific (Singapore), (1994) p. 199.

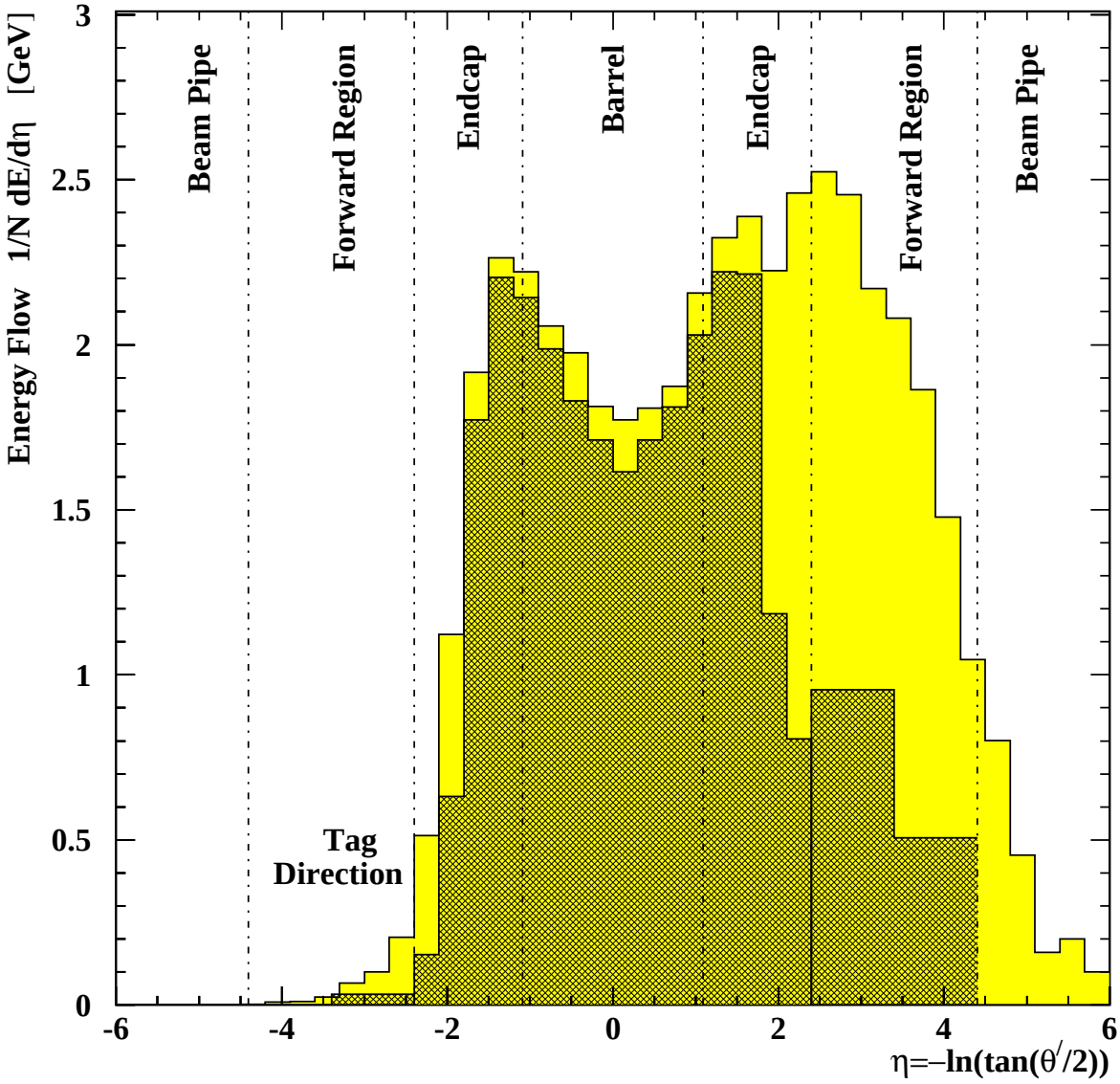

Figure 2: The hadronic energy flow per event based on the HERWIG generator as a function of the pseudorapidity η in the low-Q^2 region. The tagged electron is not shown. It is always at negative rapidities $-3.5 < \eta < -2.8$. The dark shaded histogram represents the energy reconstructed by the OPAL detector after the simulation of the detector response to the HERWIG events. The vertical lines show the acceptance regions of the OPAL detector components. The generated energy distribution for these events is represented by the lightly shaded histogram.

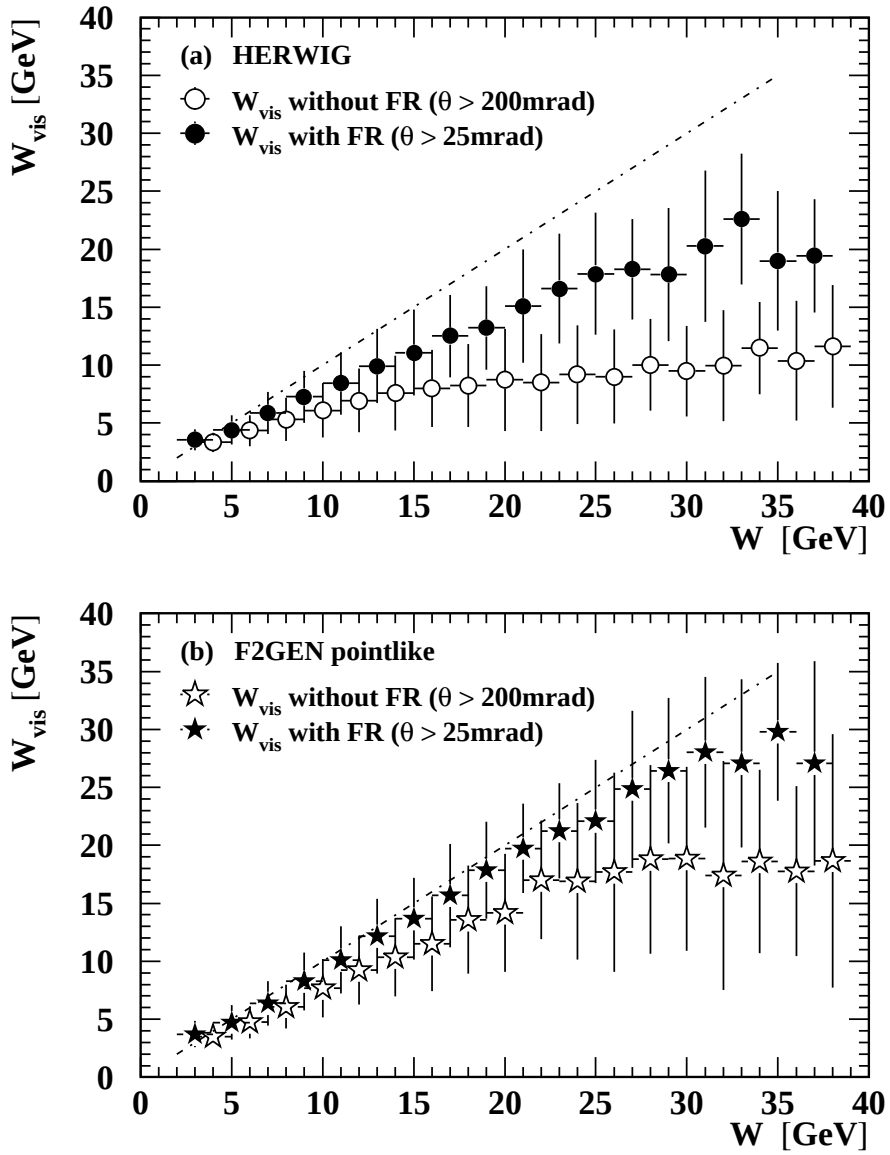

Figure 3: The correlation between the generated hadronic invariant mass W and the visible value $W_{\rm vis}$ with and without the hadronic energy sampled in the forward region (FR) of the OPAL detector. Figure (a) shows the correlation for HERWIG and (b) the correlation for F2GEN; in each case for two cuts on the minimum polar angle of the acceptance region. $\theta > 25$ mrad means that the energy of the forward region is included, whereas $\theta > 200$ mrad indicates that the detectors in the forward region are not used in the calculation of $W_{\rm vis}$. The symbols show the average $W_{\rm vis}$ in each bin, and the vertical error bar its standard deviation. The dashed line represents $W_{\rm vis} = W$.

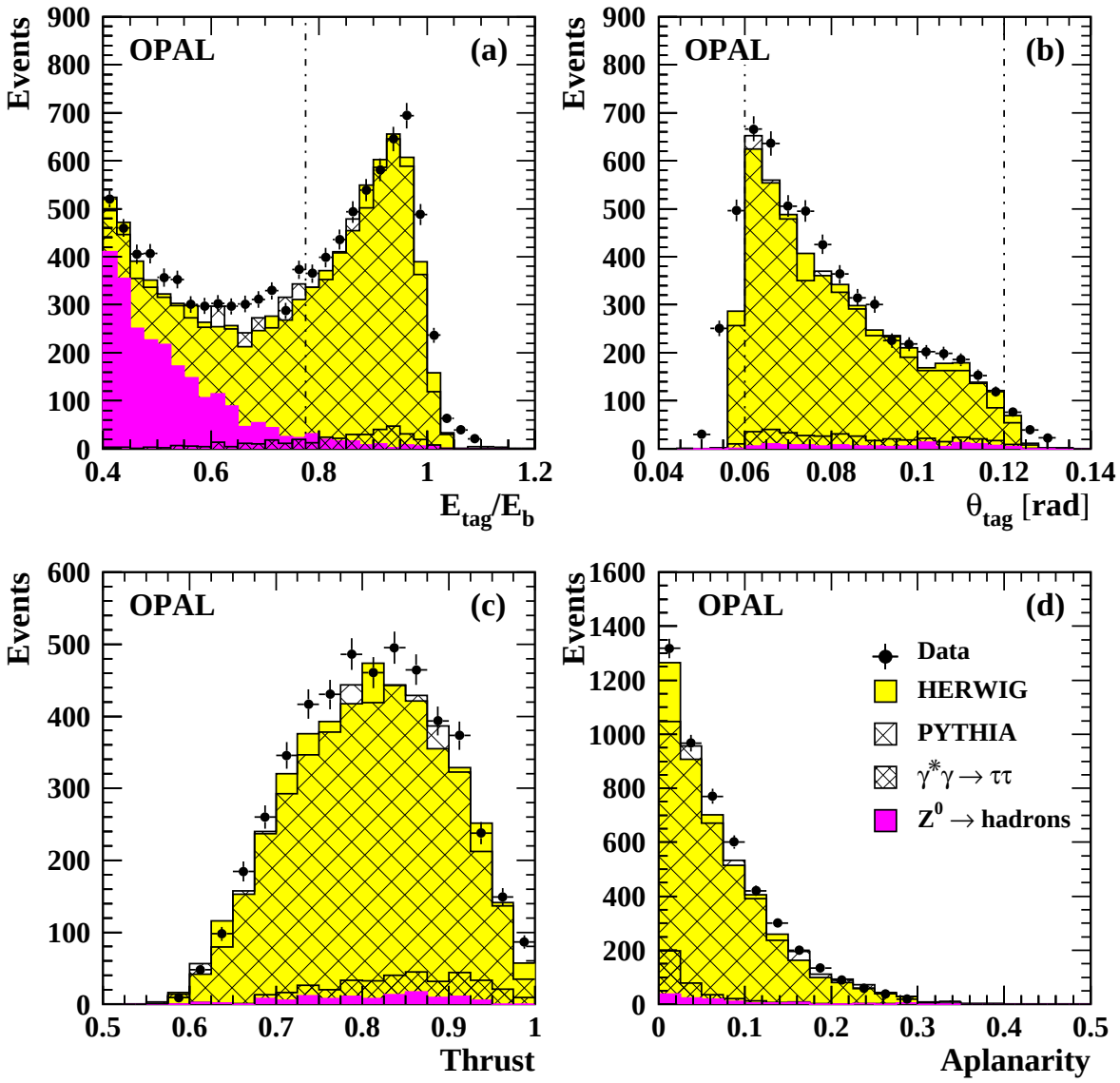

Figure 4: Comparison of data event quantities in the low-Q^2 region with the HERWIG and PYTHIA Monte Carlo models which have been normalised to the luminosity of the data. In figure (a) and (b) all cuts listed in section 3 are applied, except the one on the variable shown. In figures (c) and (d) all cuts are applied. The vertical lines in figure (a) and (b) indicate the cut values. The backgrounds from $\gamma^\star\gamma \to \tau^+\tau^-$ and $Z^0 \to$ hadrons events, which are also shown separately at the bottom, have been added to the HERWIG and PYTHIA Monte Carlo samples. Thrust and aplanarity are calculated in the laboratory frame. All errors are statistical only.

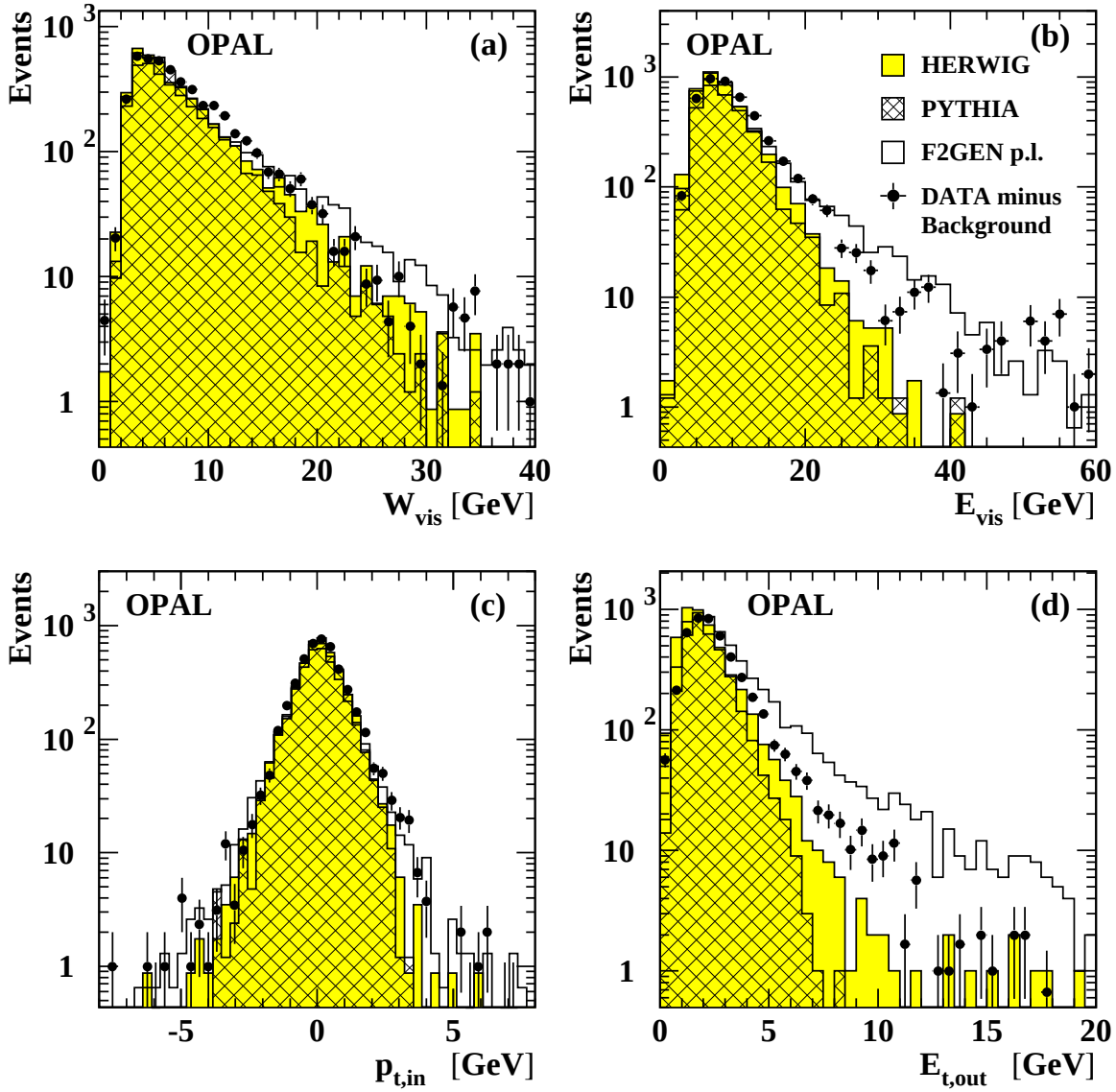

Figure 5: Comparison of data event quantities in the low-Q^2 region with HERWIG, PYTHIA and F2GEN pointlike (p.l.) Monte Carlo samples. (a) the distribution of the visible invariant mass, (b) the total visible energy of the event, (c) the transverse momentum of the event in the tag plane, (d) the energy out of the tag plane. The tag plane is defined by the beam direction and the direction of the tagged electron.

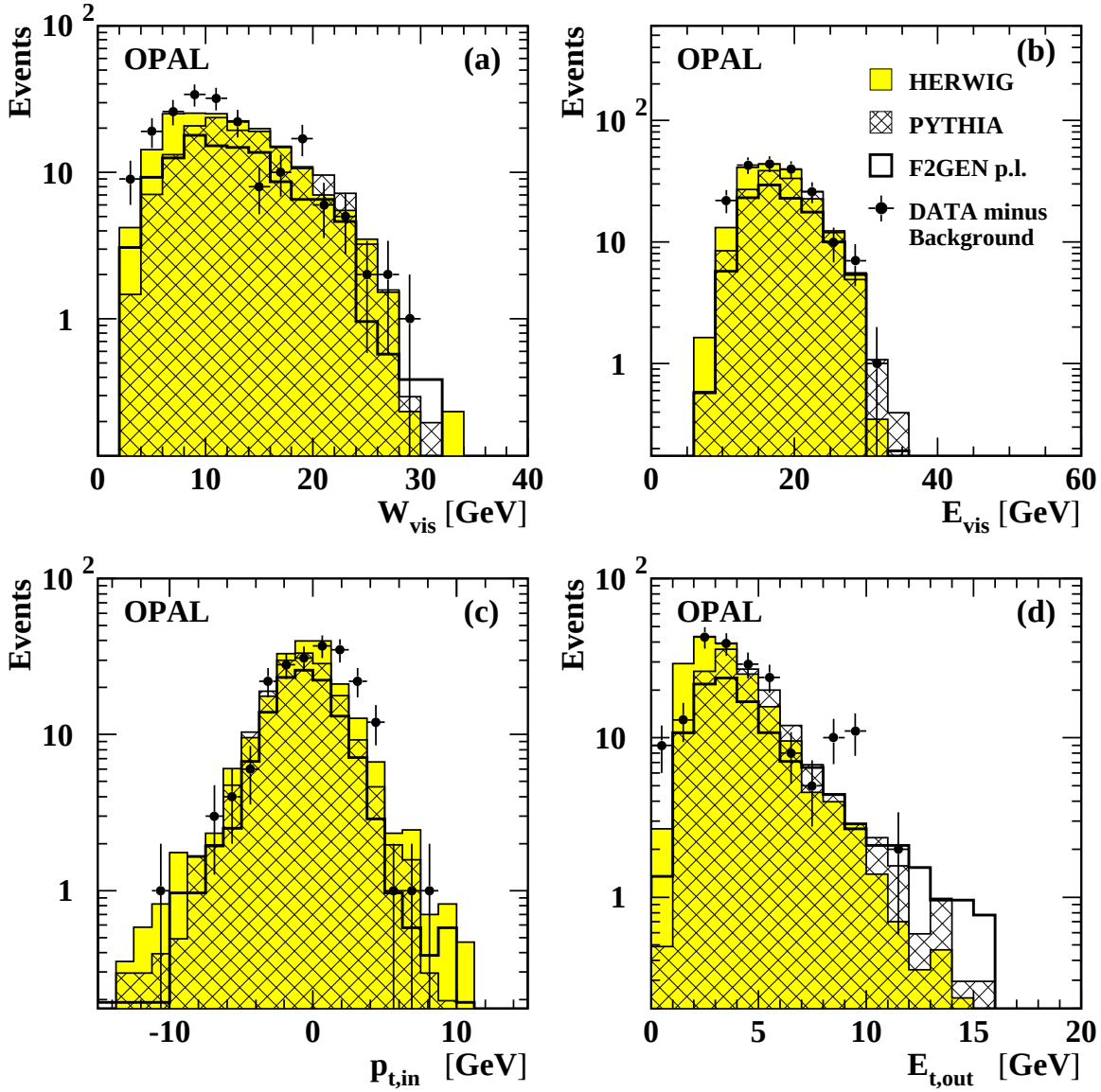

Figure 6: Comparison of data event quantities in the high-Q^2 region with HERWIG, PYTHIA and F2GEN pointlike (p.l.) Monte Carlo samples. (a) the distribution of the visible invariant mass, (b) the total visible energy of the event, (c) the transverse momentum of the event in the tag plane, (d) the energy out of the tag plane. The tag plane is defined by the beam direction and the direction of the tagged electron.

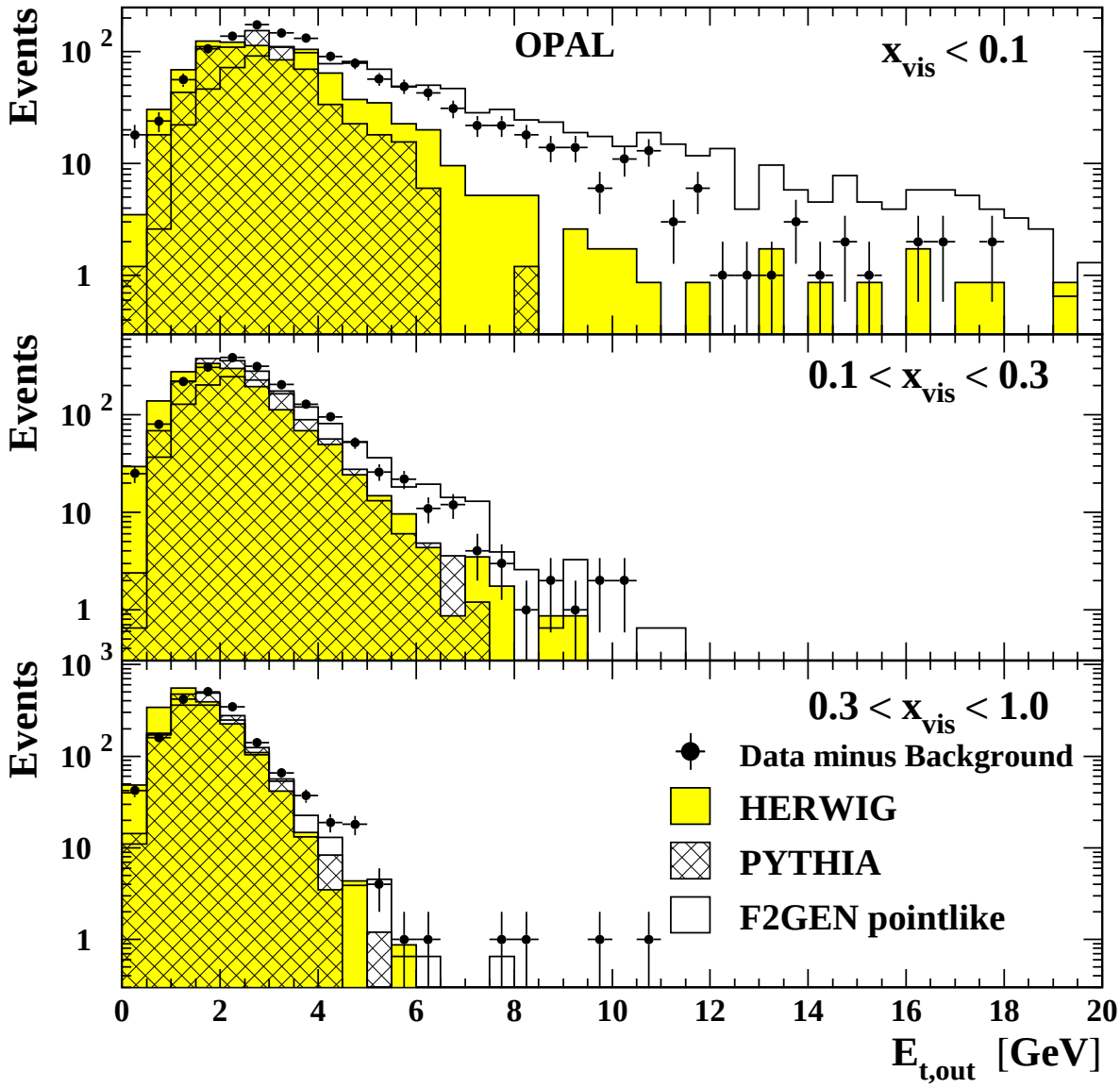

Figure 7: The energy transverse to the plane defined by the beam axis and the tag direction for three ranges in $x_{\rm vis}$, for events in the low-Q^2 region.

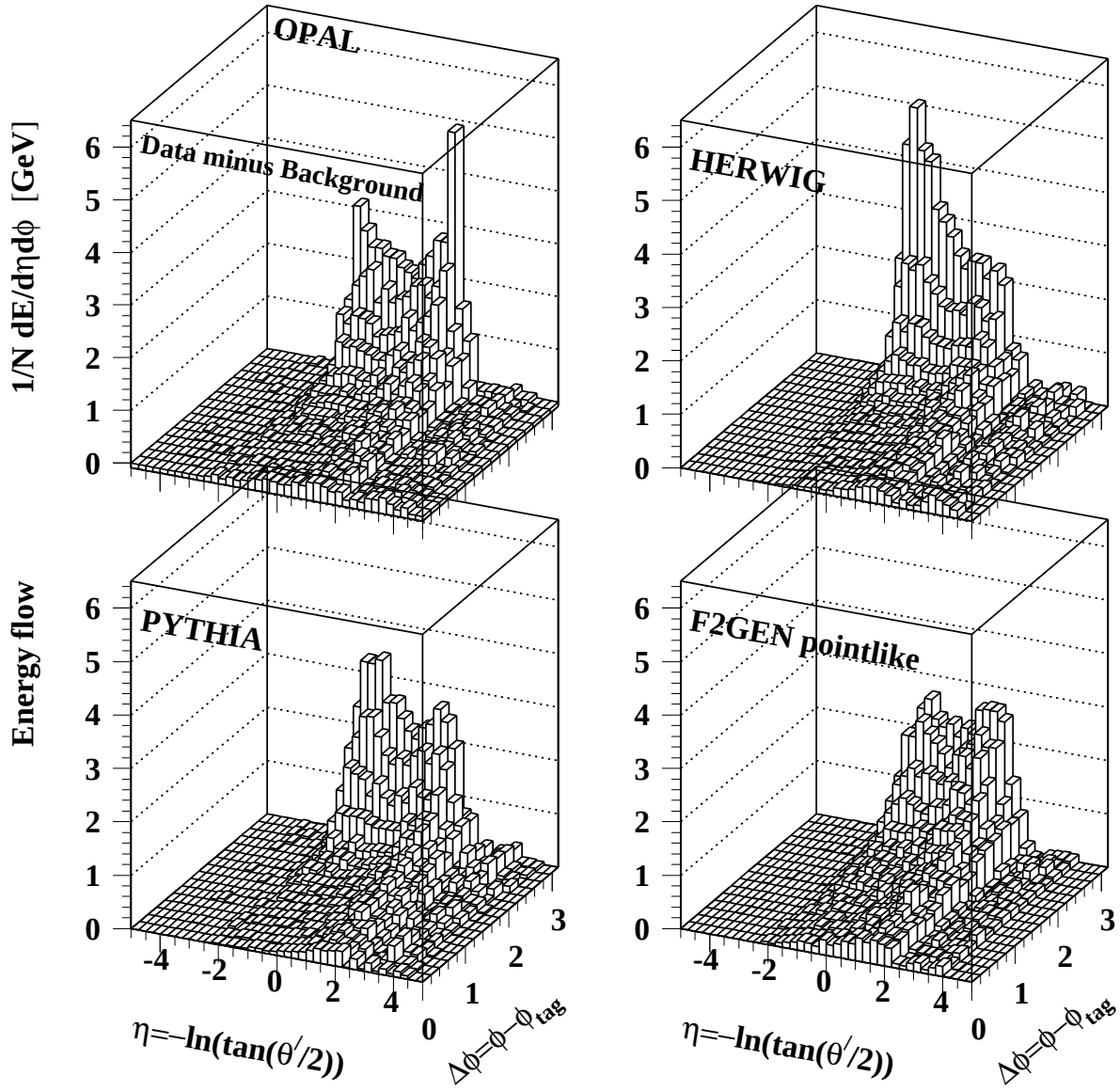

Figure 8: The hadronic energy flow per event in the low-Q^2 region as a function of pseudorapidity η and $\Delta\phi$. θ' is the polar angle measured from the side opposite to the tagged electron, which is always at negative η and at $\Delta\phi$=0.

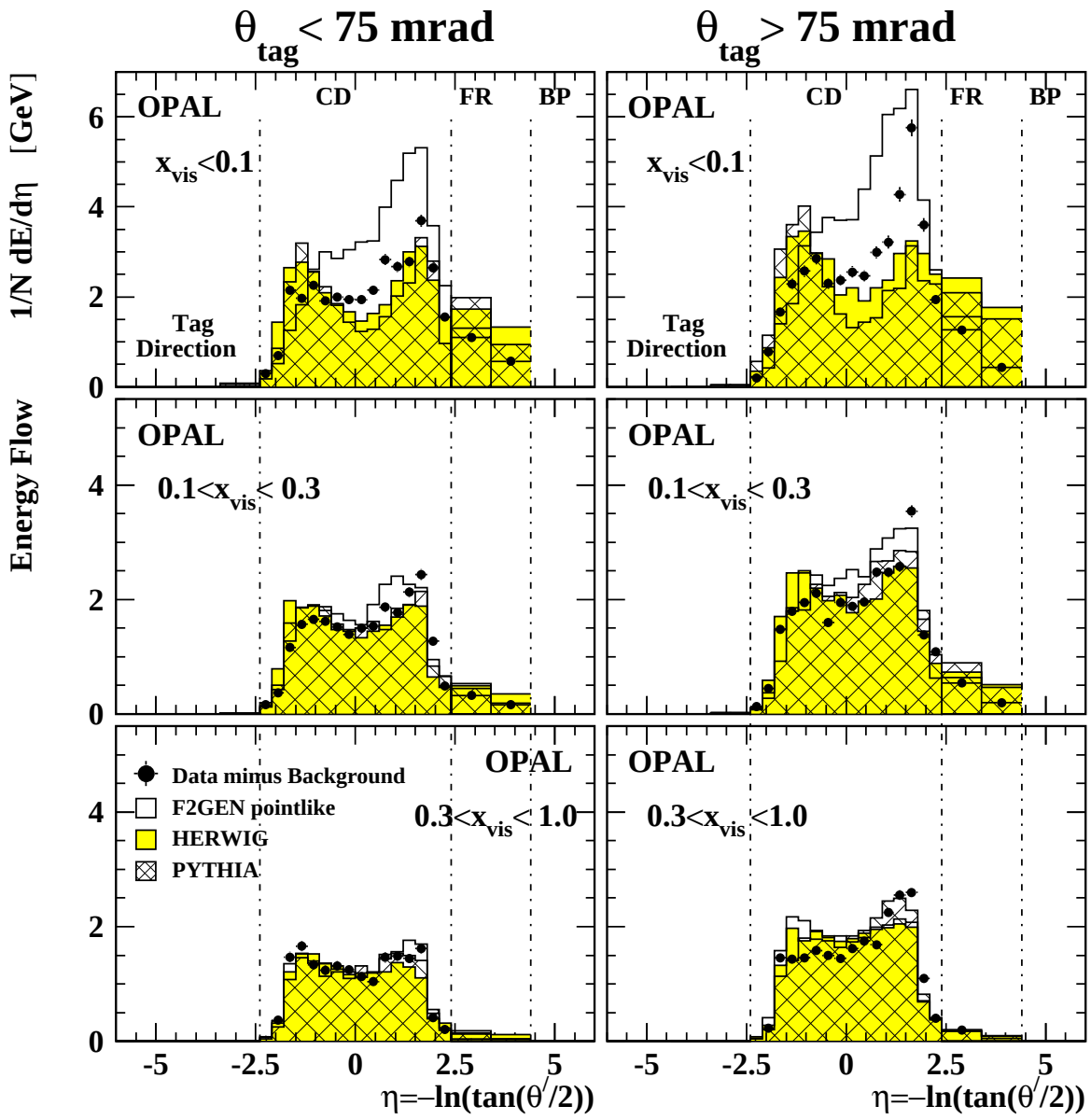

Figure 9: The hadronic energy flow per event as a function of pseudorapidity η for the data and various signal Monte Carlo samples. The energy flow is shown for various ranges of $x_{\rm vis}$ and $\theta_{\rm tag}$ for the low-Q^2 sample. The errors shown are statistical only. The vertical lines show the acceptance regions of the OPAL detector components. CD = Central Detector (including the barrel and endcaps), FR = Forward Region and BP = Beam Pipe.

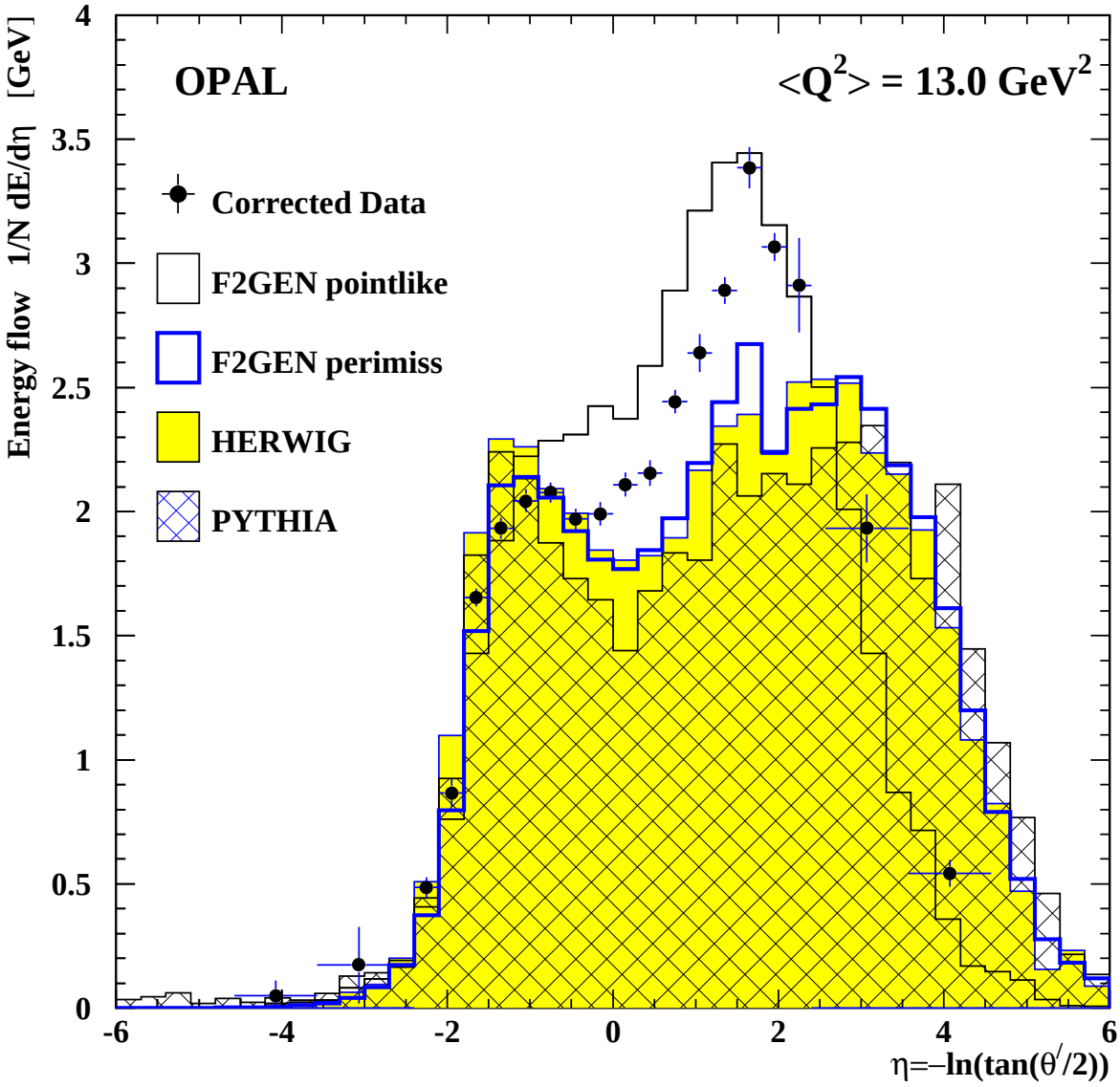

Figure 10: The measured energy flow per event in the low-Q^2 region, corrected for the detector inefficiencies, as a function of pseudorapidity η, compared to the generated energy flow of the HERWIG and PYTHIA Monte Carlo models and the energy flow of samples of pointlike and perimiss events from the F2GEN model. The vertical error bars on the data points are the sum of the statistical and systematic errors, and the horizontal bars indicate the bin widths. Note the different bin width in the forward regions.

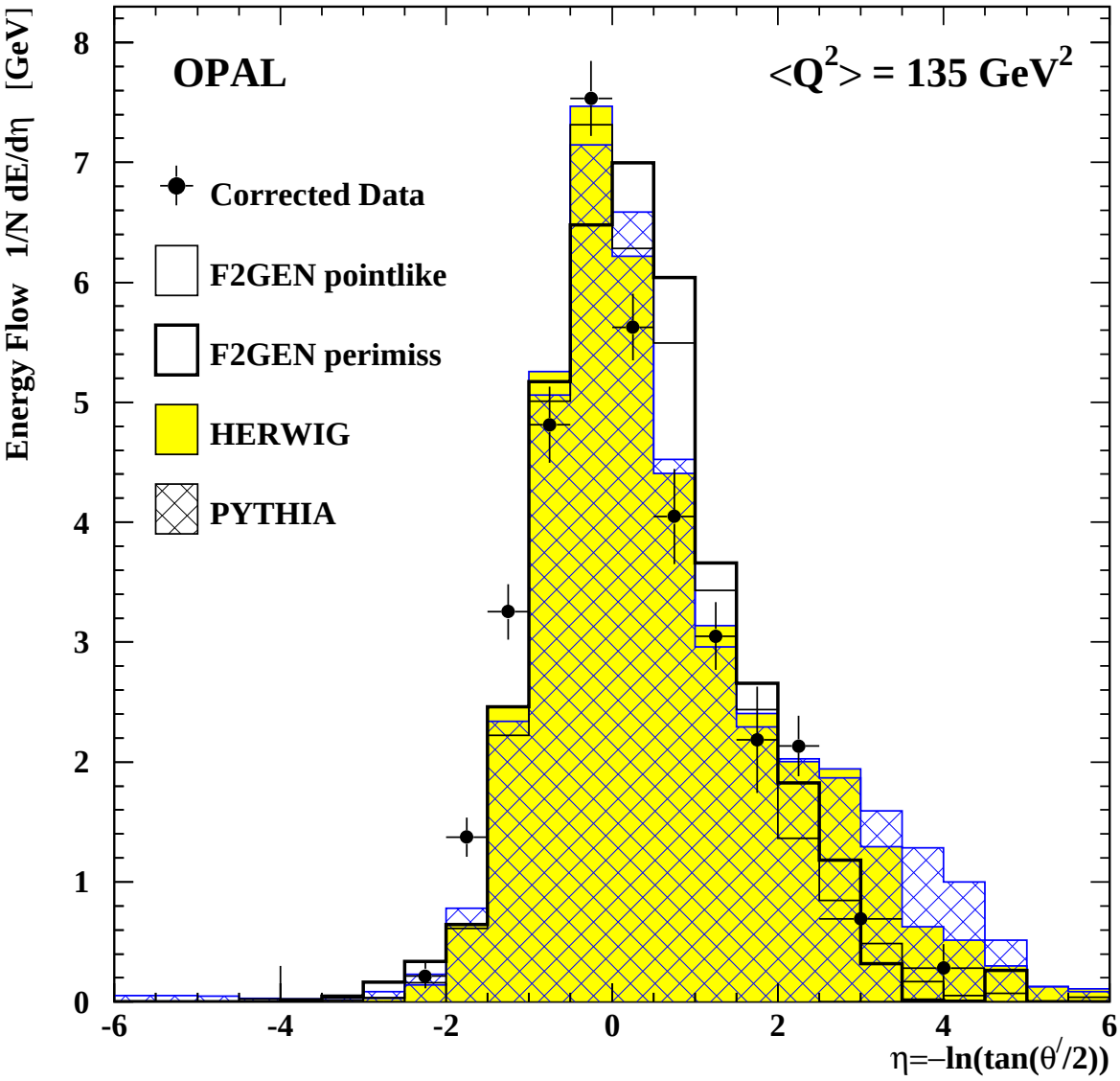

Figure 11: The measured energy flow per event in the high-Q^2 region, corrected for the detector inefficiencies, as a function of pseudorapidity η, compared to the generated energy flow of the HERWIG and PYTHIA Monte Carlo models and the energy flow of a sample of pointlike and perimiss events from the F2GEN model. The vertical error bars on the data points are the sum of the statistical and systematic errors, the horizontal bars indicate the bin widths. Note the different bin width in the forward regions.

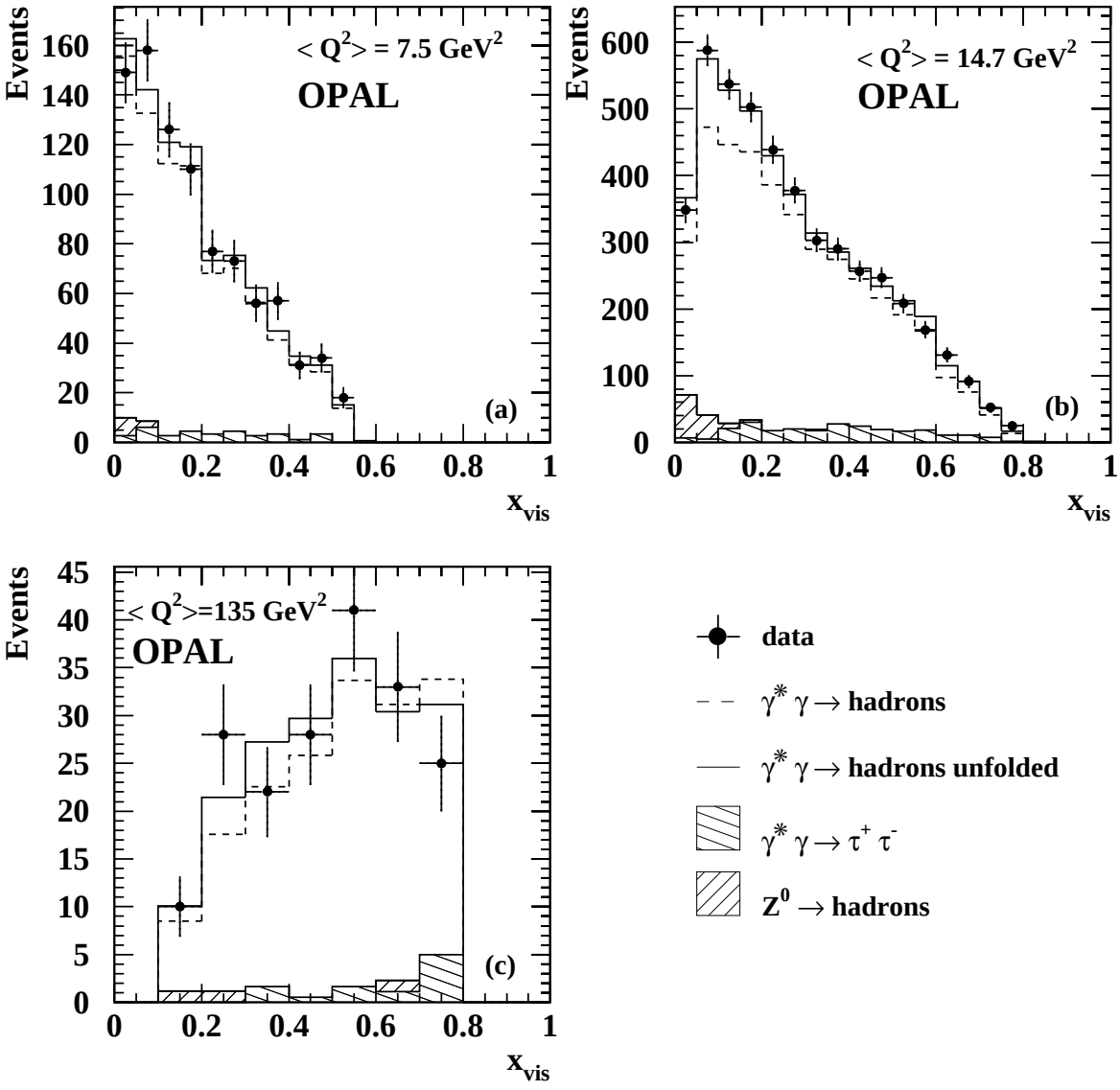

Figure 12: The distribution of $x_{\rm vis}$ for various mean momentum transfers $\langle Q^2 \rangle$. The dashed histogram shows the events from the HERWIG Monte Carlo, using the GRV parametrisation and the standard cuts, with the background events added to it, before the unfolding; the solid histogram shows the same quantity after the unfolding has been performed. The background events from $\gamma^\star\gamma \to \tau^+\tau^-$ and $\mathrm{Z}^0 \to$ hadrons are also shown separately at the bottom of the figure. All errors shown are statistical only.

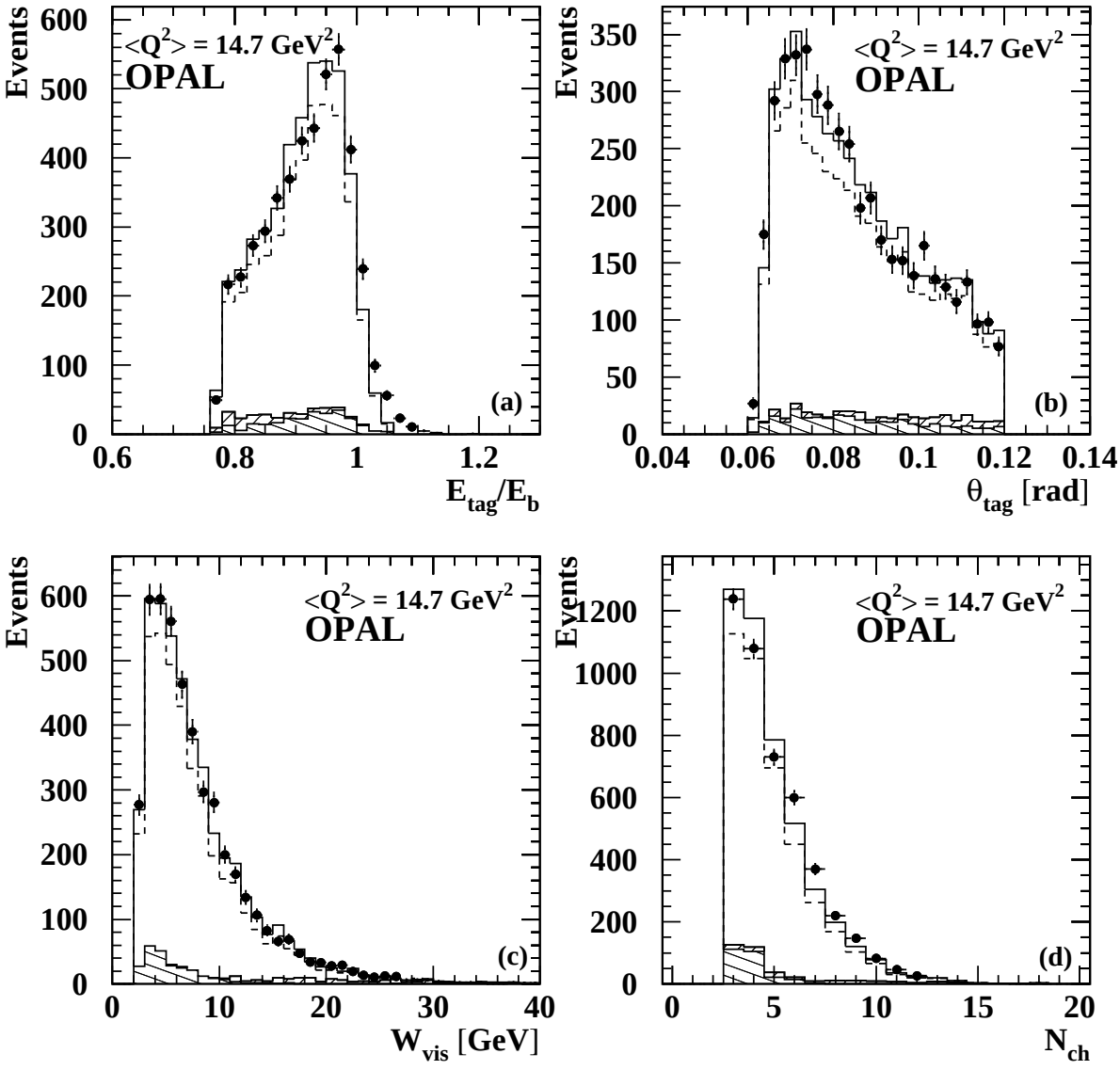

Figure 13: Distributions of measured quantities compared to the HERWIG Monte Carlo, using the GRV parametrisation and the standard cuts, for $\langle Q^2 \rangle = 14.7$ GeV^2. The variables shown are (a) the energy of the tagged electron as a fraction of the beam energy, (b) the polar angle of the tagged electron, (c) the visible invariant mass of the hadronic system, and (d) the number of charged particles seen in the detector. The meaning of the symbols is as defined in figure 12.

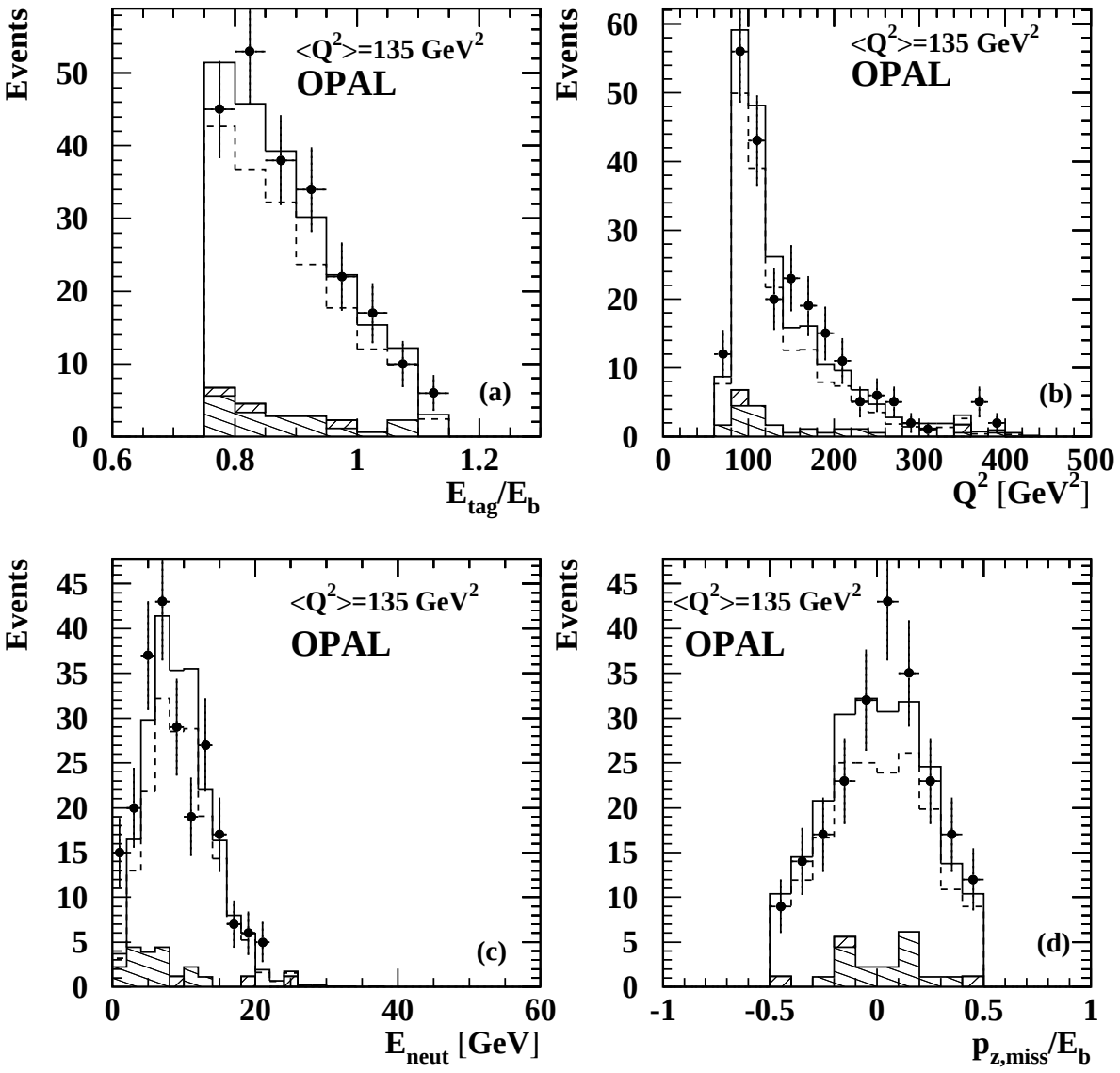

Figure 14: Distributions of measured quantities compared to the PYTHIA Monte Carlo, using the SaS1D parametrisation and the standard cuts, for $\langle Q^2 \rangle = 135$ GeV^2. The variables shown are (a) the energy of the tagged electron as a fraction of the beam energy, (b) the measured Q^2, (c) the measured neutral energy, and (d) the missing longitudinal momentum of the event scaled by the beam energy. The meaning of the symbols is as defined in figure 12.

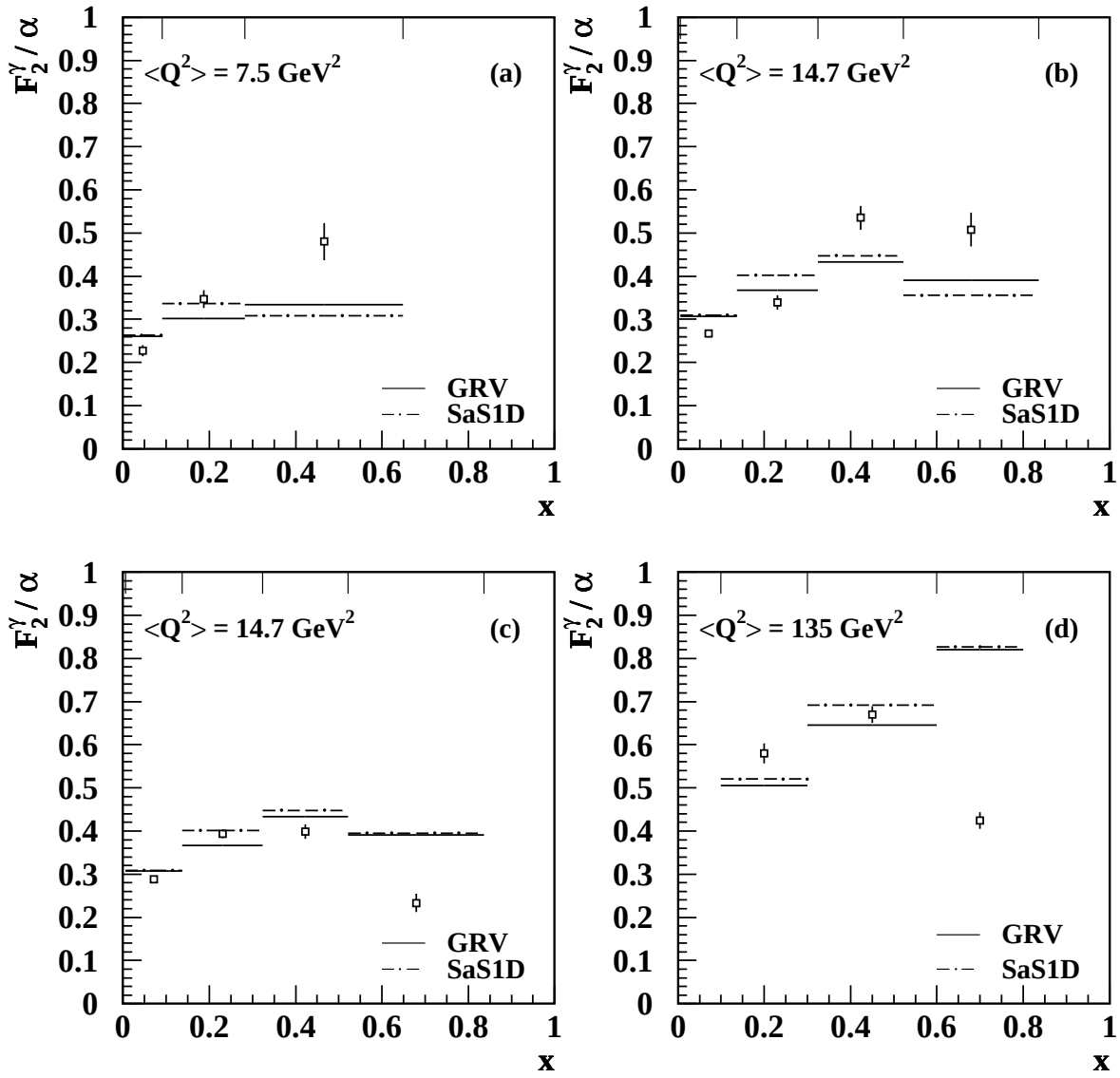

Figure 15: Unfolding tests using different Monte Carlo models to mimic the data (see text for further details). In (a) and (b) HERWIG, and in (c) and (d) PYTHIA are used to generate the mock data samples, always with the SaS1D parton density parametrisation. The model used to unfold the mock data is based on the reference sample as explained in the text. This sample uses the GRV parametrisation. The horizontal lines represent the mean F_2^γ of the samples in each bin. The dash-dotted lines represent the F_2^γ based on the SaS1D parton density parametrisation and the solid lines represent the F_2^γ based on the GRV parton density parametrisation. The points show the result of the unfolding of the mock data. The errors shown are statistical only. The vertical lines at the top of the figure indicate the bin sizes.

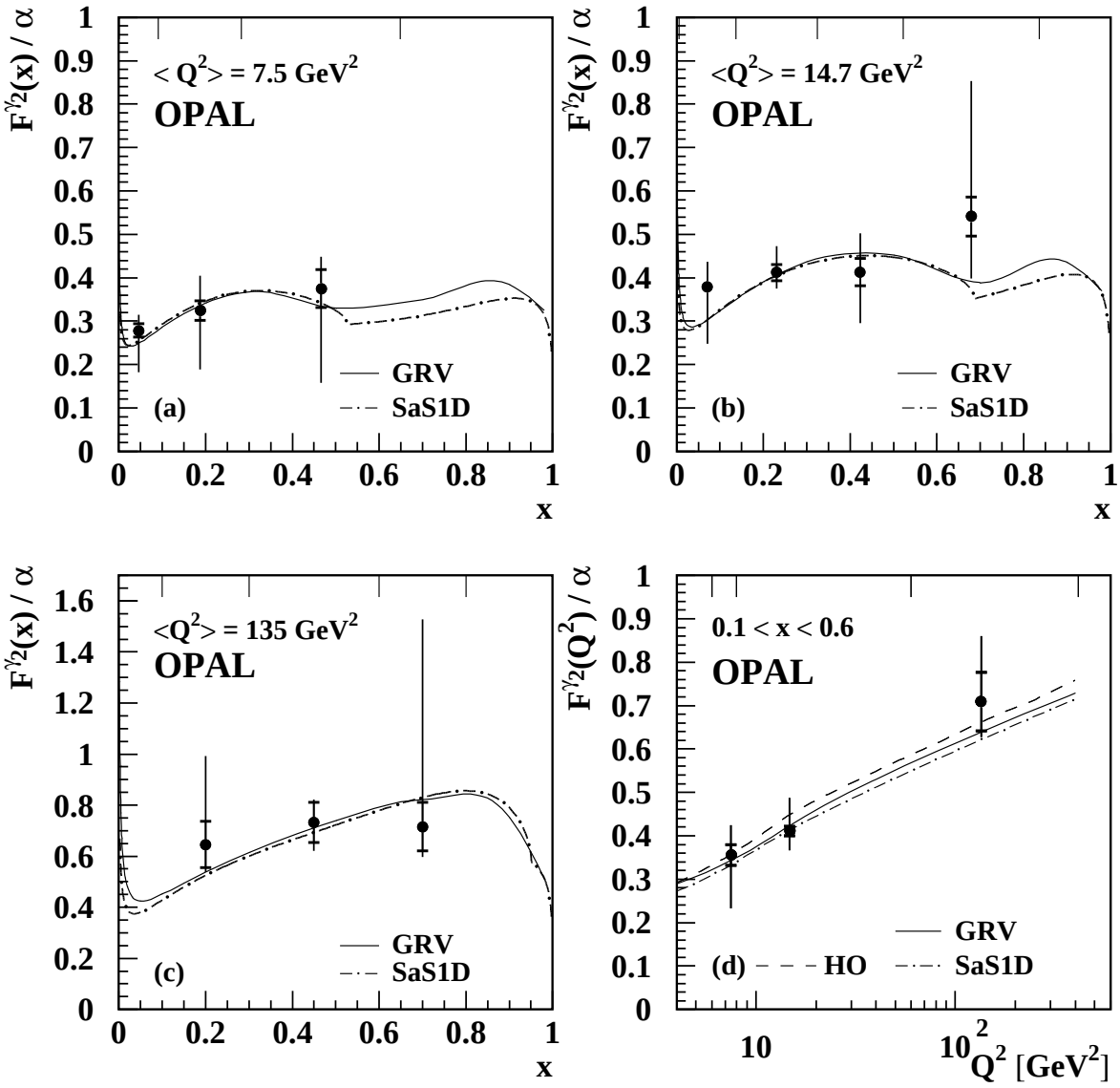

Figure 16: The measurement of F_2^γ for four active flavours for three values of $\langle Q^2 \rangle$, (a) $\langle Q^2 \rangle = 7.5$ GeV^2, (b) $\langle Q^2 \rangle = 14.7$ GeV^2, (c) $\langle Q^2 \rangle = 135$ GeV^2, and (d) the evolution of F_2^γ as a function of Q^2 for the x range $0.1 < x < 0.6$. The points show the measured F_2^γ. The bin sizes are indicated by the vertical lines at the top of the figure. The solid line represents the F_2^γ derived from the GRV parametrisation and the dash-dotted line denotes the F_2^γ derived from the SaS1D parametrisation, both using the Bethe-Heitler contribution to F_2^γ for massive charm quarks. The charm mass m_c is taken to be 1.3 GeV and 1.5 GeV in the case of SaS1D and GRV, respectively. The dashed curve labeled HO in (d) is a higher order prediction explained in the text.